Laplace surface dynamics, revisited: satellites, exoplanets, and debris with distant, eccentric companions

Mohammad Farhat, Jihad Touma

▶ **To cite this version:**

Mohammad Farhat, Jihad Touma. Laplace surface dynamics, revisited: satellites, exoplanets, and debris with distant, eccentric companions. Monthly Notices of the Royal Astronomical Society, 2021, 507 (4), pp.6078-6093. ⟨10.1093/mnras/stab2490⟩. ⟨hal-03468379⟩

HAL Id: hal-03468379

https://hal.science/hal-03468379v1

Submitted on 20 Apr 2023

HAL is a multi-disciplinary open access archive for the deposit and dissemination of scientific research documents, whether they are published or not. The documents may come from teaching and research institutions in France or abroad, or from public or private research centers.

L'archive ouverte pluridisciplinaire **HAL**, est destinée au dépôt et à la diffusion de documents scientifiques de niveau recherche, publiés ou non, émanant des établissements d'enseignement et de recherche français ou étrangers, des laboratoires publics ou privés.

HAL Authorization

Monthly Notices of the ROYAL ASTRONOMICAL SOCIETY

MNRAS **507,** 6078–6093 (2021) https://doi.org/10.1093/mnras/stab2490
Advance Access publication 2021 September 2

Laplace surface dynamics, revisited: satellites, exoplanets, and debris with distant, eccentric companions

Mohammad A. Farhat [1,2]★ and Jihad R. Touma [2,3]★

[1] *IMCCE, CNRS, Observatoire de Paris, PSL University, Sorbonne Université, 77 Avenue Denfert-Rochereau, F-75014 Paris, France*
[2] *Department of Physics, American University of Beirut, PO Box 11-0236, Riad El-Solh, Beirut 11097 2020, Lebanon*
[3] *Center for Advanced Mathematical Sciences, American University of Beirut, PO Box 11-0236, Riad El-Solh, Beirut 11097 2020, Lebanon*

Accepted 2021 August 18. Received 2021 July 19; in original form 2021 July 19

ABSTRACT

To date, studies of Laplace surface dynamics have concerned themselves with test particle orbits of fixed shape and orientation in the combined field of an oblate central body (to which the particle is bound) and a distant, inclined companion, which is captured to quadrupolar order. While amply sufficient for satellites around planets on near-circular orbits, the quadrupolar approximation fails to capture essential dynamical features induced by a wide binary companion (be it a star, a planet, or a black hole) on a fairly eccentric orbit. With similar astronomical settings in mind, we extend the classical Laplace framework to higher multipoles and map out the backbone of stationary orbits, now made complex by the broken axial symmetry. Eccentric and inclined Laplace equilibria, which had been presaged in systems of large enough mutual inclination, are here delineated over a broad range of mutually inclined perturbations. We recover them for test particles in the field of a hot Jupiter and a wide eccentric stellar binary, highlighting their relevance for the architecture of multi-planet systems in binaries. We then extend and deploy our machinery closer to home, as we consider the secular dynamics of trans-Neptunian objects (TNOs) in the presence of a putative ninth planet. We show how generalized Laplace equilibria seed islands for trans-Neptunian objects to be sheltered around, islands within chaotic seas that we capture via Poincaré sections, while highlighting a beautiful interplay between Laplace and Kozai–Lidov secular dynamical structures. An eminently classical tale revived for the exoplanetary 21st century!

Key words: gravitation – celestial mechanics – Kuiper belt: general – planets and satellites: dynamical evolution and stability.

1 INTRODUCTION

The orbital architecture of planetary satellites provides the ideal astronomical setting in which to explore hierarchical dynamical processes, combining the effects of planetary oblateness on the inside and the solar tide on the outside. In that setting, the existence of a 'proper' inclination, at which the circular orbit of a satellite around an oblate and oblique planet is stationary, was recognized by Laplace (1805) in his classic study of Jupiter's satellites. That peculiar inclined plane, which is now referred to as the Laplace plane, approaches the planet's equator on the inside and tends to the planet's orbit around the Sun with increasing orbital radius. This single-parameter family of Laplace planes is enveloped by a surface that interpolates as it warps between the equator and the orbit of the planet. It is naturally referred to as the *Laplace surface*, an idealized object of persistent fascination, which has structured our understanding of the formation and evolution of planetary satellites and accompanying ring systems for more than two hundred years now.

With a view to greater realism and consequent complexity, Tremaine, Touma, and Namouni (2009, TTN hereafter) relaxed the assumption of circular equilibria and studied the stability of the classic Laplace surface to perturbations in a satellite's eccentricity. They thus opened a can of worms and left the field with a series of novel results, touching primarily on highly oblique planets and including a hitherto unsuspected instability and the likelihood of stints of chaotic evolution in the course of orbital migration. Their study foresaw and ushered in a stream of exoplanetary applications and generalizations, allowing for warps of discs in binaries (Charnoz et al. 2018), warps in circumplanetary discs (Zanazzi & Lai 2016), then non-gravitational perturbations such as radiation pressure on dust grains (Tamayo et al. 2013; Rosengren & Scheeres 2014). The circle was recently closed back to the Solar system, when it was realized that an origin around a fast-spinning and oblique Earth, which is favored on geochemical grounds, could generate a Moon with a Laplace plane that may very well be prone to TTN's eccentricity instability (Ćuk et al. 2016, 2021; Tian & Wisdom 2020)!

The present work begins where TTN left the Laplace surface and relaxes yet another assumption in the original Laplace story by accounting explicitly for an eccentric binary companion, thus effectively breaking the hitherto assumed axisymmetry of the outer perturber. This level of generality is again demanded by exoplanetary systems, the discs that generate them, and remnant debris discs, all in the presence of a massive wide binary companion on an eccentric (and inclined) orbit. It is a remarkable result of secular celestial mechanics that the symmetry-breaking effect of eccentricity appears first at the octupolar order, and it is at and above that order that our calculations will be conducted.

Our formalism and associated results are of broad applicability, over a range of systems and scales. Following general results on the classical Laplace surface and its fate, we illustrate securely

★ E-mail: mohammad.farhat@obspm.fr (MAF); jt00@aub.edu.lb (JRT)

© 2021 The Author(s)
Published by Oxford University Press on behalf of Royal Astronomical Society

Downloaded from https://academic.oup.com/mnras/article/507/4/6078/6362616 by CNRS user on 20 April 2023

hierarchical regimes with a multiplanet system in a wide eccentric binary. We then overcome the breakdown of hierarchy as we explore the peculiar orbital architecture of trans-Neptunian objects (TNOs) in the presence of a putative ninth planet (Trujillo & Sheppard 2014; Batygin et al. 2019). In so doing, we generalize the planar structure studied by Beust (2016) then Saillenfest et al. (2017) to mutually inclined perturbers, as we map families of inclined, eccentric Laplace equilibria in the presence of Solar system giants (inner quadrupole forcing) and an eccentric inclined binary companion (hypothesized ninth planet). Families of equilibria and their intricate bifurcations provide the desired skeletal structure with which to explore this intriguing scenario and variations around it properly, whether allowing for the combined effect of secular and mean motion resonances (Malhotra, Volk & Wang 2016) or the combined effect of a distant inclined planetary core and a self-gravitating debris disc (Silsbee & Tremaine 2018; Sefilian & Touma 2019).

The context lends itself naturally to an interpolation between relatively strong inner quadrupolar forcing (and associated outer Kozai–Lidov dynamics) followed by relatively strong outer multipolar forcing (and associated eccentric Kozai–Lidov cycling), with the unfolding of Laplace equilibria in between. However, we are getting ahead of ourselves! So, without further ado, we shall start where we must, with the Hamiltonian governing the orbit-averaged dynamics of the infamous test particle in the elegant vectorial formalism.

2 LAPLACE SURFACE DYNAMICS: MODEL AND VARIATIONS

We are interested in the motion, specifically the relative orbital equilibria, of a test particle in the combined gravitational field of a central point particle and an inner (quadrupolar), then outer (octupolar) perturber, as reflected in the Hamiltonian $H_\mathrm{p} = H_\mathrm{K} + \Phi_\mathrm{i} + \Phi_\mathrm{o}$, with

$$H_\mathrm{K} = \frac{1}{2}\dot{\boldsymbol{r}}^2 - \frac{GM}{r}, \tag{1}$$

$$\Phi_\mathrm{i}(r,\theta) = \frac{GMQ_2}{r^3}P_2(\cos\theta) = \frac{GMQ_2}{2r^5}\left[3(\boldsymbol{r}\cdot\hat{n}_p)^2 - r^2\right], \tag{2}$$

and

$$\Phi_\mathrm{o}(\boldsymbol{r},\boldsymbol{r}') = \frac{-GM_\mathrm{o}}{r'}\left[1 + \frac{\boldsymbol{r}\cdot\boldsymbol{r}'}{r'^2} - \frac{r^2}{2r'^2} + \frac{3(\boldsymbol{r}\cdot\boldsymbol{r}')^2}{2r'^4} + \frac{5}{2}\frac{(\boldsymbol{r}\cdot\boldsymbol{r}')^3}{r'^6} - \frac{3}{2}\frac{\boldsymbol{r}\cdot\boldsymbol{r}'}{r'^4}r^2 + ...\right]. \tag{3}$$

Under H_K alone, a bound test particle, with position vector $\boldsymbol{r}$ and velocity vector $\dot{\boldsymbol{r}}$, evolves on a spatially fixed Keplerian ellipse in the central force field of a Newtonian point particle of mass M. We do not have reasons to consider general relativistic (read post-Newtonian) corrections in this work, though it should be quite straightforward and interesting to explore their signature in future instalments.

Inner to the test particle's orbit, $\Phi_i(\boldsymbol{r}, \hat{n}_\mathrm{p})$ models a non-spherical mass distribution, here captured up to quadrupolar order, essentially an axisymmetric gravitational perturbation of strength Q_2 and axis of symmetry $\hat{n}_\mathrm{p}$. Outside that same orbit, we envisage a point particle of mass M_o bound to the central body with position vector $\boldsymbol{r}'$ (on a fairly eccentric Keplerian orbit) and perturbing the test particle with potential $\Phi_\mathrm{o}(\boldsymbol{r},\boldsymbol{r}') = -GM_\mathrm{o}/|\boldsymbol{r}-\boldsymbol{r}'|$, here captured to octupolar order.

Classically, the central body stands for the monopolar contribution of a planet (Jupiter, say) and the inner quadrupole for that planet's dominant departure from spherical symmetry, namely the effect of its equatorial bulge. The strength $Q_2 = J_2R_\mathrm{p}^2$ of that bulge (R_p being the planet's radius and J_2 its gravitational second zonal harmonic) can be amended further with the contribution of a system of inner satellites with mass and semi-major axis $\{m_i, a_i\}$, $i = 1...n$:

$$Q_2' = Q_2 + \frac{1}{2}\sum_{i=1}^{n}\frac{a_i^2 m_i}{M}, \tag{4}$$

here all assumed to revolve on circular orbits in the planet's equatorial plane.

The outer body is then typically the star hosting the planetary system in question (say the Sun), and its perturbative effect in a hierarchical architecture is often limited to quadrupolar order, at which any orbital eccentricity appears as a parameter affecting the strength of perturbation to that order (more on that below).

This, in particular, is the context in which Laplace and followers worked, the same model around which TTN elaborated their generalization to eccentric Laplace equilibria. That context was further applied to a range of astrophysical settings, allowing for variations on the central body (a host star in a wide binary system), the inner quadrupole (a hot Jupiter, a system of planets), the outer perturber (a binary companion, a distant planet), and the test particle (a planet in a hierarchical arrangement, a particle in a debris disc).

By accounting for higher order contributions from the outer perturber, we take a first, and already quite challenging, step towards breaking the implicit axisymmetry of the classical model. The aim is to identify the skeletal structure of surviving eccentric, inclined Laplace equilibria, when sufficient allowance is made for the outer perturber's lopsided mass distribution.

To get anywhere close to recovering those novel equilibria, we will need to proceed, as did others before us, by averaging the model Hamiltonian, with all the caveats associated with that averaging, whether allowing for orbital resonances or contributions from higher order effects in mildly hierarchical systems. It is our belief that the skeleton that we map out will provide a secure scaffolding for dynamical insights, then further generalizations and modifications.

With a view to developments that follow, we introduce an orbital reference frame with the following triad:

(i) $\hat{n}$ in the direction of the test particle's orbital angular momentum,
(ii) $\hat{u}$ in the direction of the periapse of the orbit,
(iii) $\hat{v} = \hat{n} \times \hat{u}$.

The frame is of course fixed for unperturbed particle motion that takes place in the $(\hat{u}, \hat{v})$ plane and osculates with the orbit in the presence of perturbations, which are here assumed small in comparison with the pull of the central body. Bound Keplerian orbital motion is given by

$$r = \frac{a(1-e^2)}{1+e\cos(f)}, \qquad \boldsymbol{r} = r[\cos(f)\,\hat{u} + \sin(f)\,\hat{v}], \tag{5}$$

where a and e are the particle's semi-major axis and eccentricity, r the orbital radius, and v the true anomaly relative to $\hat{u}$.

Secular dynamical evolution is then captured by time-averaging any Hamiltonian contributions over a period $P = 2\pi/\sqrt{GM/a^3}$ on the particle's osculating Keplerian orbit. In so doing, it is useful to keep in mind the following differential relations:

$$\frac{\mathrm{d}t}{P} = \frac{r\,\mathrm{d}E}{2\pi a} = \frac{r^2\,\mathrm{d}f}{2\pi ab} = \frac{\mathrm{d}M}{2\pi}, \tag{6}$$

where $b = a\sqrt{1-e^2}$ is the semi-minor axis, E the eccentric anomaly, and M the mean anomaly.

Downloaded from https://academic.oup.com/mnras/article/507/4/6078/6362616 by CNRS user on 20 April 2023

Similar expressions are used when averaging further over the mean anomaly of the outer perturber, assumed to be on an eccentric Keplerian orbit with position vector $\boldsymbol{r}'$, semi-major axis and eccentricity $a_{\rm o}$ and $e_{\rm o}$, respectively, and reference triad $\hat{n}_{\rm o},\ \hat{u}_{\rm o},\ \hat{v}_{\rm o}$.

The secular test-particle dynamics is then best parametrized with the normalized angular momentum vector, $\boldsymbol{j}=\sqrt{1-e^2}\hat{n}$, and the Lenz vector, $\boldsymbol{e}=e\hat{u}$, thus avoiding singularities of Keplerian orbital elements at zero eccentricity and/or inclination. Recovering expressions for orbit-averaged multipoles in terms of those vectorial elements is a straightforward though somewhat laborious exercise, which is now well documented in various publications on hierarchical triples (e.g. Tremaine et al. 2009; Correia et al. 2011; Hamers 2020). With these and similar works for reference, we simply quote the doubly averaged Hamiltonian associated with $H_{\rm p}$:

$$H_{\rm S}=-\frac{GM}{2a}+\frac{GM}{a}\Psi, \tag{7}$$

with $\Psi=\Psi_{\rm p}+\Psi_{\rm quad}+\Psi_{\rm oct}$ and

$$\begin{aligned}
\Psi_{\rm p}&=\frac{\varepsilon_{\rm p}}{4(1-e^2)^{5/2}}\left[1-e^2-3(\boldsymbol{j}\cdot\hat{n}_{\rm p})^2\right],\\
\Psi_{\rm quad}&=\frac{3\varepsilon_{\rm o}}{8}\left[\frac{1}{3}-2e^2+5e_n^2-j_n^2\right],\\
\Psi_{\rm oct}&=\frac{15}{64}\varepsilon_{\rm o}\varepsilon_{\otimes}\left[e_u\left(8e^2-1-35e_n^2+5j_n^2\right)+10j_uj_ne_n\right],
\end{aligned} \tag{8}$$

with dimensionless parameters given by

$$\varepsilon_{\rm p}=\frac{Q_2'}{a^2};\qquad \varepsilon_{\rm o}=\frac{M_{\rm o}a^3}{Ma_{\rm o}^3\left(1-e_{\rm o}^2\right)^{3/2}};\qquad \varepsilon_{\otimes}=\frac{e_{\rm o}}{1-e_{\rm o}^2}\frac{a}{a_{\rm o}}. \tag{9}$$

Subscripts appended to j and e reflect base vectors on which $\boldsymbol{j}$ and $\boldsymbol{e}$, respectively, are projected.

Along with TTN, we remind the reader that, in our model Hamiltonian, the following holds: (1) the inner quadrupole is spatially fixed, a valid assumption when the precession rate is negligibly slow; (2) the particle of interest is massless; (3) the test particle is far enough from the inner perturber that its potential can be approximated as a quadrupole; (4) the outer perturber is sufficiently hierarchical (and eccentric) for its tide to be reasonably approximated in the adopted octupolar expansion, and at the same time sufficiently far from the inner perturber to neglect their mutual perturbation and resulting precession (refer to the discussion section below for further elaborations on perturber precession); (5) finally, the obvious: namely, the perturbations are weak enough for the dynamics to be captured reasonably well in the secular orbit averaged framework.

2.1 Equations of motion

Secular dynamics of the test particle is dictated by $H_{\rm S}$. This Hamiltonian is cyclic in the particle's mean anomaly, thus the momentum conjugate to that anomaly, $\sqrt{GMa}$, is conserved, and with it the semi-major axis of the orbit. The orbit's orientation and shape are then fully controlled by the evolution of $\boldsymbol{e}$ and $\boldsymbol{j}$. We follow Allan & Cook (1964) and Tremaine et al. (2009) in writing the vectorial equations of motion generated by the orbit-averaged Hamiltonian of equation (7):

$$\begin{aligned}
\frac{{\rm d}\boldsymbol{j}}{{\rm d}\tau}&=-\boldsymbol{j}\times\nabla_j\Psi-\boldsymbol{e}\times\nabla_e\Psi,\\
\frac{{\rm d}\boldsymbol{e}}{{\rm d}\tau}&=-\boldsymbol{e}\times\nabla_j\Psi-\boldsymbol{j}\times\nabla_e\Psi,
\end{aligned} \tag{10}$$

with $\tau=\sqrt{(GM/a^3)}t$. Expanding, we obtain

$$\begin{aligned}
\frac{{\rm d}\boldsymbol{j}}{{\rm d}\tau}&=\frac{3}{4}\varepsilon_{\rm o}j_n\boldsymbol{j}\times\hat{n}_{\rm o}-\frac{15}{4}\varepsilon_{\rm o}e_n\boldsymbol{e}\times\hat{n}_{\rm o}+\frac{3}{2}\varepsilon_{\rm p}\frac{(\boldsymbol{j}\cdot\hat{n}_{\rm p})}{(1-e^2)^{5/2}}\boldsymbol{j}\times\hat{n}_{\rm p}\\
&\quad-\frac{75}{64}\varepsilon_{\rm o}\varepsilon_{\otimes}\left[\left[2\left(e_uj_n+e_nj_u\right)\boldsymbol{j}+2\left(-7e_ne_u+j_uj_n\right)\boldsymbol{e}\right]\times\hat{n}_{\rm o}\right.\\
&\quad\left.+\left[2e_nj_n\boldsymbol{j}+\left(-7e_n^2+j_n^2+\frac{8}{5}e^2-\frac{1}{5}\right)\boldsymbol{e}\right]\times\hat{u}_{\rm o}\right],
\end{aligned} \tag{11}$$

$$\begin{aligned}
\frac{{\rm d}\boldsymbol{e}}{{\rm d}\tau}&=\frac{3}{4}\varepsilon_{\rm o}j_n\boldsymbol{e}\times\hat{n}_{\rm o}-\frac{15}{4}\varepsilon_{\rm o}e_n\boldsymbol{j}\times\hat{n}_{\rm o}+\frac{3}{2}\varepsilon_{\rm p}\frac{(\boldsymbol{j}\cdot\hat{n}_{\rm p})}{(1-e^2)^{5/2}}\boldsymbol{e}\times\hat{n}_{\rm p}\\
&\quad+\left[\frac{3}{2}\varepsilon_{\rm o}-\frac{3}{4}\varepsilon_{\rm p}\frac{1-e^2-5(\boldsymbol{j}\cdot\hat{n}_{\rm p})^2}{(1-e^2)^{7/2}}\right]\boldsymbol{j}\times\boldsymbol{e}-\frac{75}{64}\varepsilon_{\rm o}\varepsilon_{\otimes}\\
&\quad\times\left[\left[2\left(e_uj_n+e_nj_u\right)\boldsymbol{e}+2\left(-7e_ue_n+j_uj_n\right)\boldsymbol{j}\right]\times\hat{n}_{\rm o}\right.\\
&\quad+\left[2e_nj_n\boldsymbol{e}+\left(-7e_n^2+j_n^2+\frac{8}{5}e^2-\frac{1}{5}\right)\boldsymbol{j}\right]\\
&\quad\left.\times\hat{u}_{\rm o}+\frac{16}{5}e_u\boldsymbol{j}\times\boldsymbol{e}\right].
\end{aligned} \tag{12}$$

We pause for a few remarks before getting down to business.

(i) *The octupole.* Terms involving $\varepsilon_{\otimes}$ reflect the octupolar perturbation by the eccentric outer body. The eccentricity of that body was already present at the quadrupolar level, but only as a constant factor through an averaged contribution independent of the perturber's angular orientation. Here, that orientation is explicit through $\hat{u}_{\rm o}$.

(ii) *Symmetry breaking.* With orientation-dependent terms, the octupole breaks symmetries that were present at the quadrupolar level. In particular, the equations of motion are no longer invariant when flipping the eccentricity vector $\boldsymbol{e}\to-\boldsymbol{e}$. Further flipping $\boldsymbol{j}\to-\boldsymbol{j}$ takes the equations from $\frac{{\rm d}\boldsymbol{j}}{{\rm d}\tau}\to-\frac{{\rm d}\boldsymbol{j}}{{\rm d}\tau}$, $\frac{{\rm d}\boldsymbol{e}}{{\rm d}\tau}\to-\frac{{\rm d}\boldsymbol{e}}{{\rm d}\tau}$, and one can restore invariance through time reversal, $\tau\to-\tau$. Orbitwise, this is equivalent to taking $i\to\pi-i$, $\omega\to\pi-\omega$, $\Omega\to\Omega+\pi$.

(iii) *The principal plane.* Following TTN, we define the plane with normal oriented along $\hat{n}_{\rm p}\times\hat{n}_{\rm o}$ as the principal plane and we denote the angle between those two vectors by Θ. Classically, this angle measures the obliquity of an oblate planet, but it can be generalized to the mutual inclination between the perturbations, whatever the system. Invariance under $\hat{n}_{\rm o}\to-\hat{n}_{\rm o}$ implies that, for a full parametric study, we can restrict Θ to the range $[0,\pi/2]$ instead of $[0,\pi]$.

(iv) *Equilibria.* TTN distinguished between *coplanar–coplanar* and *coplanar–orthogonal* equilibria. In the former, both $\boldsymbol{j}$ and $\boldsymbol{e}$ lie in the principal plane, while, in the latter, one of the vectors is in the plane and the other orthogonal to it. In our case, and with the added complexity of the perturber's orientation, it was already challenging enough to study the *coplanar–coplanar* configuration in all its glory, so we left other potential configurations for investigations to follow. Furthermore, we solve for *coplanar–coplanar* in the simplest configuration where $\hat{n}_{\rm o},\ \hat{u}_{\rm o}$, and $\hat{n}_{\rm p}$ are in the same plane. Concerns about this condition will, we hope, be assuaged in the discussion below.

(v) *Stability.* When we speak of the stability of relative/Laplace equilibria of the dynamical system above, we are mainly referring to linear stability, which is assessed by considering linearized dynamics around equilibrium angular momentum and eccentricity vectors. The procedure is straightforward and will not be spelled out explicitly here. For the circular equilibria of the quadrupolar limit, TTN were able to differentiate between stability to perturbations in eccentricity and angular momentum, making use of the decoupling of the linearized equations. It was thus possible for them to derive elegant analytical expressions for the eigenvalues. With the octupole at play,

Downloaded from https://academic.oup.com/mnras/article/507/4/6078/6362616 by CNRS user on 20 April 2023

the decoupling is no longer feasible, and we resort to solving for the eigenvalues of the relevant 6×6 matrix numerically. We tested our linear stability toolbox by confronting our generalized framework with TTN's results, then confirming the linear stability results with direct integration of the full equations of motion in the neighbourhood of equilibria.

3 WHITHER THE LAPLACE SURFACE?

For equilibria of interest to us here, those fulfilling the *coplanar–coplanar* condition described above, all vectors $\hat{n}_{\rm p}$, $\hat{n}_{\rm o}$, $\hat{u}_{\rm o}$, $\boldsymbol{j}$, and $\boldsymbol{e}$ are assumed to lie on the same principal plane. In this configuration, the nodes of the planes of all three players are aligned: the mutually inclined inner and outer perturber and the test particle in between. Also, the argument of the apse of the outer perturber is assumed frozen at 90° from the ascending node on the plane of the inner perturber. In this case, equilibrium conditions for a spatially frozen test particle orbit are deduced from equations (11) and (12), as they reduce to two scalar equations for two unknowns, the orbital eccentricity e and the inclination angle between $\boldsymbol{j}$ and $\hat{n}_{\rm p}$, which we denote by ϕ. They are given by

$$\begin{aligned} 0 = {} & \frac{3}{4}\varepsilon_{\rm p}\left(1-e^2\right)^{-3/2}\sin\left(2\phi\right) - \frac{3}{8}\varepsilon_{\rm o}\left(1+4e^2\right)\sin 2\Delta\phi \\ & \mp\frac{75}{64}\varepsilon_{\rm o}\varepsilon_{\otimes}e\Bigg[-\frac{7}{2}\left(1+e^2\right)\cos\Delta\phi\sin 2\Delta\phi \\ & +\left(2+5e^2\right)\sin^3\Delta\phi + \frac{1}{5}\left(1-8e^2\right)\sin\Delta\phi\Bigg], \end{aligned} \tag{13}$$

$$\begin{aligned} 0 = {} & \frac{3}{4}\varepsilon_{\rm p}\frac{e}{\left(1-e^2\right)^2}\left(1-3\cos^2\phi\right) - \frac{3}{4}\varepsilon_{\rm o}e\sqrt{1-e^2}\left(1-4\sin^2\Delta\phi\right) \\ & \mp\frac{75}{64}\varepsilon_{\rm o}\varepsilon_{\otimes}\left(1-e^2\right)^{1/2}\Bigg[\left(3e^2-1\right)\cos^3\Delta\phi \\ & +\left(\frac{1}{5}-\frac{24}{5}e^2\right)\cos\Delta\phi + \left(1+\frac{15}{2}e^2\right)\sin\Delta\phi\sin 2\Delta\phi\Bigg], \end{aligned} \tag{14}$$

where $\Delta\phi = \Theta - \phi$. We distinguish between equilibria that are aligned and those that are anti-aligned with the external perturber's periapse. The two differ by the sign of the octupole terms, with the upper sign delivering the aligned configuration.

3.1 Destroying the classical Laplace surface: the octupole at work

Considering circular equilibria, ones with $e = 0$, octupolar terms vanish from the angular momentum equilibrium condition (13) leaving quadrupolar terms, while the opposite happens in the Lenz vector equation (14):

$$0 = 2\varepsilon_{\rm p}\sin(2\phi) - \varepsilon_{\rm o}\sin 2\Delta\phi, \tag{15a}$$

$$0 = \varepsilon_{\rm o}\varepsilon_{\otimes}\cos\Delta\phi\left(-3\cos^2\Delta\phi + \frac{11}{5}\right). \tag{15b}$$

Solutions to those equations remain quite rich and are captured succinctly in Fig. 1. In what follows, we highlight key features.

(i) In the quadrupolar limit studied by TTN[1] (equation 15a), circular equilibria fall into two families:

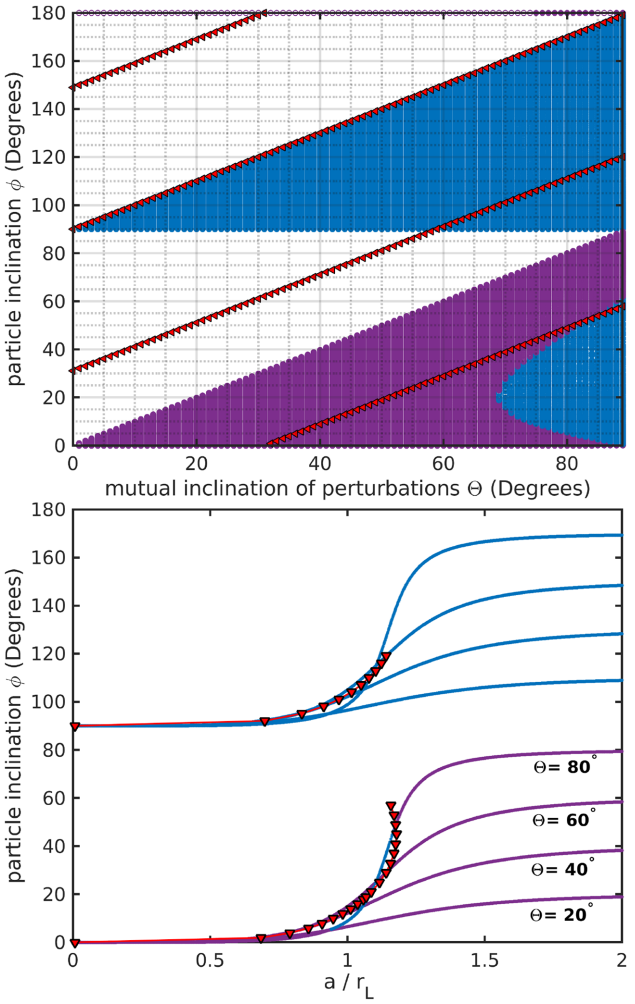

Figure 1. Inclinations of circular coplanar–coplanar Laplace equilibria. *Top*: equilibrium inclination as a function of the mutual inclination between the inner quadrupole and the outer eccentric perturber ($e_o = 0.65$). Purple (stable) and blue (unstable) orbits satisfy the relative equilibrium conditions in the quadrupolar limit (equation 15a). Designated by red triangles, on top of the quadrupolar solutions, are pairs that satisfy the condition introduced by the octupole (equation 15b). Pairs overlapping with the quadrupolar shaded regions are the survivors of the classical Laplace surface upon the octupolar addition. *Bottom:* inclinations of circular equilibria, now mapped as a function of semi-major axis, for a range of mutual inclinations ($\Theta = 20, 40, 60, 80°$). A color version of this figure is available in the online journal.

(a) a stable family that runs between $\phi = 0$ as $a \to 0$ and $\phi \to \Theta$ as $a \to \infty$, forming the classical Laplace surface. This transition between perturbation planes occurs around the Laplace radius given by

$$r_{\rm L}^5 = Q_2' a_{\rm o}^3\left(1-e_{\rm o}^2\right)^{3/2}\frac{M}{M_{\rm o}} = a^5\frac{\varepsilon_{\rm p}}{\varepsilon_{\rm o}}. \tag{16}$$

TTN showed how circular Laplace equilibria on the classical Laplace surface become unstable over a range of inclinations and semi-major axes around the Laplace radius. This occurs

[1]While with TTN, we point out minor typographical errors in their equations (22)–(23). While the first equality in either equation is correct as stated, the algebraically reduced form is not. In the second equality of TTN's equation (22), the minus in the denominator should be a plus. In the denominator of the second equality in TTN's equation (23), the minus should be a plus, and 1 should be replaced with $\cos 2\phi_{\odot}$ in their notation.

Downloaded from https://academic.oup.com/mnras/article/507/4/6078/6362616 by CNRS user on 20 April 2023

when Θ exceeds a critical value of 68.875°. In the top panel of Fig. 1, we reproduce TTN's stable equilibria in purple, in the range $\phi = 0 \ldots \phi_o$, enclosing the blue zone of unstable equilibria.

(b) Also shown in blue are TTN's unstable retrograde equilibria, running between $\phi = \pi/2$ as $a \to 0$ and $\phi \to \Theta + \pi/2$ as $a \to \infty$. In the second panel of Fig. 1, TTN's prograde and retrograde families are shown as a function of semi-major axis, for four different mutual inclinations between the perturbations ($\Theta = 20, 40, 60, 80°$).

(ii) When we account for the eccentricity of the outer perturber through the octupole terms, classical Laplace equilibria are further constrained by the additional condition in equation (15b), which imposes

$$\cos\Delta\phi = 0 \qquad \text{or} \qquad \cos\Delta\phi = \pm\sqrt{\frac{11}{15}}. \tag{17}$$

Orbits satisfying this additional condition are displayed in red together with the quadrupolar solution in Fig. 1. With the octupole in action, surviving circular equilibria are given by those red dots that overlap with the shaded regions. As shown in the second panel of Fig. 1, classical families of equilibria now collapse into discrete equilibrium orbits, each corresponding to a distinct mutual inclination. Consequently, the warped Laplace surface, traditionally running over the full range of semi-major axes, is now destroyed and replaced by a distinguished family of circular orbits. It is interesting to note that surviving prograde circular equilibria would cease to exist beyond $a = 1.17 r_{\rm L}$, namely when entering the eccentric perturber dominated regime. We also note that the structure of surviving relative equilibria is independent of the eccentricity of the outer perturber.

(iii) Though the destruction of structure requiring symmetry is perhaps not surprising, the fact that circular equilibria survive this eccentric perturbation surely is. Those survivors carry the same stability signature as the quadrupolar regions they fall on. Even more curious, perhaps, is the surviving family with $\Delta\phi = 31.09°$: a family of circular orbits that, independent of the eccentricity of the outer perturber, are fixed in space with a constant tilt to the angle of mutual inclination between the perturbations.

3.2 The emergence of the eccentric Laplace surface

Having explored what remains of the classical Laplace surface, we now characterize the structure that replaces it by mapping the full set of equilibria in the coplanar–coplanar configuration, without any prior constraint on eccentricity of the test particle. When it comes to model systems, one can envisage a satellite (the test particle) orbiting an oblate planet that revolves on an eccentric orbit around a star, or a multi-planetary system where the inner quadrupole is provided by an oblate star and/or coplanar inner planets, while the outer octupole is provided by an eccentric inclined distant Jupiter or a stellar binary companion. We proceed with the latter scenario, and carry out the exercise for a system with an inner stellar binary component of mass 1.5 $M_\odot$ hosting a hot Jupiter of mass 0.5 M_J situated on a circular orbit at 0.1 au, with a less massive (1 $M_\odot$) outer stellar binary companion revolving on an eccentric orbit with $a_o = 180$ au and $e_o = 0.95$. We use the test particle approximation for a hypothetical planet in between the mutually inclined perturbations.

The remnant circular equilibria of Fig. 1 can then be situated within a continuum of eccentric and inclined equilibria, which is mapped in Fig. 2, then cross-sectioned in Fig. 3. As apparent in Fig. 2 (which incidentally is limited to prograde orbits), eccentric equilibria display the same warped surface structure, interpolating between inner and outer planes, as they shape the eccentric Laplace surface. Equilibrium eccentricities increase with distance from the inner host as expected, reaching values around $e \approx 0.2$ as they transition to the octupole-dominated regime. Near-circular obits occupy two distinct regions: $\mathcal{R}_1$ towards the bottom of the figure, i.e. orbits dominated by the inner quadrupole, and $\mathcal{R}_2$ around the surviving family of circular equilibria with $\Delta\phi = 31.09°$. The eccentric equilibria of TTN, those bifurcating from circular equilibria beyond 68.875°, are now part of a continuum of eccentric equilibria over the full range of mutual inclinations.

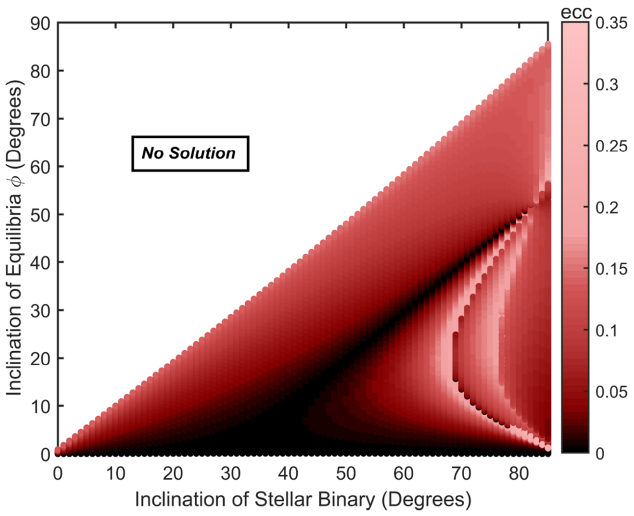

Figure 2. Inclinations of eccentric coplanar–coplanar equilibria as a function of the mutual inclination between the perturbations, with octupole included. The system studied is the multiplanetary system of Section 3.2. This figure is to be compared with the top panel of Fig. 1, corresponding to circular prograde equilibria. Similarly to the quadrupolar limit, and for each mutual inclination between the perturbations, a family of equilibria starts in the plane of the inner quadrupole at small semi-major axis, then transitions to the plane of the outer eccentric perturber. However, equilibria are now eccentric due to the outer octupole, and their eccentricity increases as a function of the semi-major axis, thus creating the eccentric Laplace surface. The colour gradient is coded for eccentricity, with darkest regions representing its smallest values, though not exactly zero. A color version of this figure is available in the online journal.

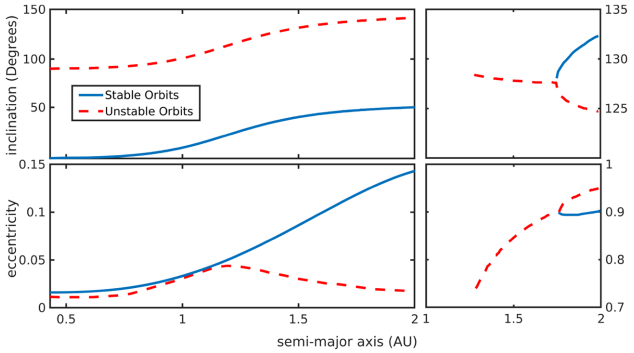

Figure 3. A sample of equilibria sectioned in Fig. 2 and mapped into (a, e) and (a, i) space. The mutual inclination between the stellar companions is 50°. Compared with the quadrupolar limit, the stable Laplace surface, along with its accompanying unstable family, is shown in the panels on the left, preserving the inclination behaviour but with eccentric stationary orbits. A highly eccentric retrograde bifurcation is evident in the panels on the right. A color version of this figure is available in the online journal.

Downloaded from https://academic.oup.com/mnras/article/507/4/6078/6362616 by CNRS user on 20 April 2023

For a perhaps more vivid appreciation of the eccentric-inclined Laplace equilibria that emerge in the presence of an eccentric outer perturber, in Fig. 3 we map equilibrium families over a range of semi-major axes (straddling the Laplace transition) and with a mutual inclination $\Theta = 50^\circ$ between perturbers. The eccentric Laplace surface is captured by the blue family in the left panels, a stable family of equilibria that transitions in inclination between the inner and outer planes (top left) as it increases in eccentricity (bottom left). In those same panels, we show how the retrograde surface is maintained with highly inclined unstable equilibria of relatively small eccentricity. In the right panels of Fig. 3, for clarity we isolate equilibrium families undergoing bifurcations of much higher eccentricity and inclination into stable and unstable branches: there is much more to say about those below, as we consider implications for the shepherding of TNOs!

In sum, and compared with TTN, the coplanar–coplanar skeleton of eccentric equilibria presented here reveals new and significant features, in both the prograde eccentric Laplace surface and the highly eccentric retrograde bifurcations. Prograde eccentric families in the quadrupolar limit of TTN are bound to two regions in $\Theta - \phi$ space: the region of circular equilibrium instability for $\Theta > 68^\circ.875$ with $0 < \phi < 54^\circ.7$, and another region where $\Theta > 54^\circ.7$ with $54^\circ.7 < \phi < 90^\circ$. Here we obtain them for the full range of mutual inclinations.

We note that we are solving for equilibria over a carefully selected range of test particle semi-major axis $0.025 < \frac{a}{a_o}\frac{1}{1-e_o^2} < 0.12$. This choice is dictated by two requirements of the multipolar secular formalism: (1) avoiding close encounters between the test particle and its perturbers on one hand, and (2) making sure to guarantee the convergence of the multipolar expansion on the other. In this work, we have very little to say on potential departures from the averaging limit, but we do consider a way around the divergence of the multipolar expansion, which yields an efficient means of exploring the full range of available secular equilibria.

4 FROM MULTIPOLES TO HARMONICS: DYNAMICS BEYOND NEPTUNE

We extend our secular machinery to dynamical systems where the multipole expansion breaks down, providing a remarkably efficient remedy to the situation. We motivate our toolbox and associated results with a problem of current interest, namely the phase-space structure inhabited by trans-Neptunian objects (TNOs), the curious orbital architecture of which motivated the hypothesis of a ninth planet in the outer parts of the Solar system. Much has been written about this curious system (Batygin & Brown 2016; Holman & Payne 2016; Batygin & Morbidelli 2017; Li et al. 2018; Batygin et al. 2019), including a contribution by one of the co-authors of this work (Sefilian & Touma 2019), and it is not our objective here to review, discuss, defend, or critique arguments or counter-arguments for one scenario or the other. Rather, we take the intellectual effort that has been exerted on the dynamics of this region of the Solar system as a pretext to develop tools and insights (of the Laplace surface variety) that we believe are of relevance to numerous other secular dynamical settings (from exoplanetary systems to black hole nuclei) where similar such mildly hierarchical structures are prevalent. The question for us reduces to the characterization of the secular orbital architecture of test particles, perturbed on the inside by the giant planets and on the outside by a putative ninth planet, a super-Earth, revolving on an eccentric and inclined orbit.

The orbital configuration of P9 is in a process of continued refinement (Batygin et al. 2019; Fienga et al. 2020). Here, we adopt

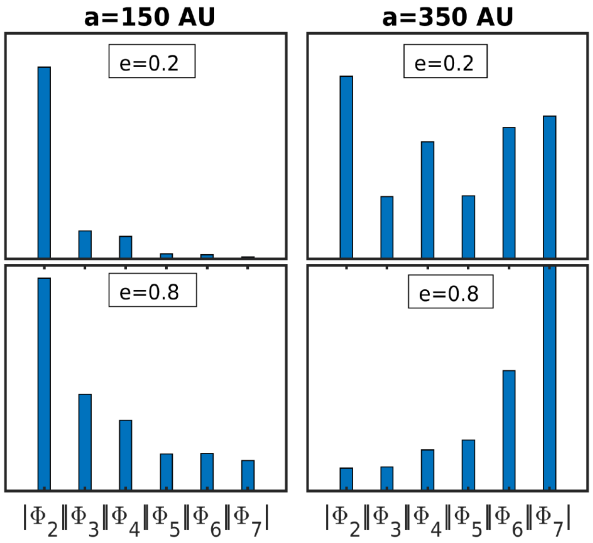

Figure 4. Numerical analysis of increasing orders in the orbit-averaged multipolar expansion of the disturbing potential of P9 up to seventh order (normalized by the quadrupole Φ_2). The potential is computed in the planar case for different orbital parameters of the test particle, with P9 at $a_9 = 700$ au and $e_9 = 0.6$. The series converges for $a = 150$ au, for which the particle's apoapse falls within the orbit-crossing limit for any eccentricity. However, the series diverges at a higher semi-major axis ($a = 400$ au), for which the apoapse falls beyond the orbit-crossing limit for both eccentricities presented. A color version of this figure is available in the online journal.

the orbital parameters first introduced in Batygin & Brown (2016), namely $a_9 = 700$ au, $e_9 = 0.6$, and a slightly inclined orbit with $i_9 = 10^\circ$. Considering this configuration (and the updates that followed), together with the distribution of TNO semi-major axes, it is evident that the hierarchy of the hypothesized system is rather weak; a multipole expansion in the ratio of the semi-major axes is expected to fail. Indeed, and as one gathers from the multipole coefficients displayed in Fig. 4, the series converges when the TNO apoapse is less than 280 au (i.e. the periapse of P9) and diverges beyond. Our conclusion is consistent with studies of the convergence of the direct part of the disturbing function (Migaszewski & Goździewski 2008, 2009) and can be expressed succinctly using

$$a(1+e) < 700(1-0.6)\ \text{au} < 280\ \text{au}. \quad (18)$$

In the model binary system we explored in Section 3.2, this limit is satisfied for the full range of semi-major axes and eccentricities considered. To overcome this hurdle in the P9 context, relatively recent works resorted to numerical averaging of the disturbing function (Beust 2016; Saillenfest et al. 2017). The approach was adopted for coplanar perturbers, though one should, in principle, be able to extend it to fully spatial interactions. It was costly to undertake in the coplanar case; it is expected to be even more so for fully triaxial configurations. Here, we adopt a somewhat more brutal approach, spreading P9's mass over the corresponding Gaussian ring (the result of averaging over P9's mean anomaly), then resolving the gravitational potential of the resulting P9 ring into spherical harmonics. Further numerical averaging of the dominant harmonics over a test particle's mean anomaly yields the desired Hamiltonian controlling the secular dynamics TNOs over the full range of eccentricity and inclination, and the range of semi-major axis of interest. The full procedure is spelled out in Appendix A.

Downloaded from https://academic.oup.com/mnras/article/507/4/6078/6362616 by CNRS user on 20 April 2023

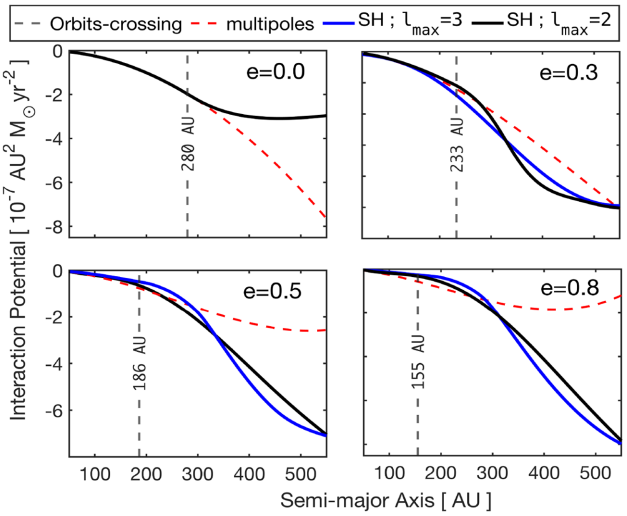

Figure 5. Comparison between P9 potentials generated by the orbit-averaged multipole expansion up to the octupole, and the orbit-averaged numerical modes expanded in spherical harmonics. We distinguish in the latter between truncating at harmonic orders $l_{\max} = 2$ and $l_{\max} = 3$. The eccentricities are for a test particle evolving in the plane of P9, apsidally anti-aligned with it and feeling its potential. For each eccentricity we identify the orbit-crossing limit defined by equation (18), beyond which P9's ring contributes from within and without and the multipole expansion diverges. The two methods agree within this limit, with the lower order harmonics yielding a better agreement. A color version of this figure is available in the online journal.

In Fig. 5, we compare averaged harmonics thus constructed with the by-now-familiar octupolar series, noting reasonable agreement for semi-major axes that avoid the orbit-crossing limit at any given eccentricity. The two approaches differ significantly, as they must, beyond that limit, with the multipolar series diverging and harmonics yielding results that approach exact quadrature, as they decay in magnitude with increasing order (Fig. A1). The difference arises from the way each approach handles the mass distribution in the perturber's ring. For a given test particle, a sound multipole expansion assumes a point-mass perturber that is either inside or outside that particle, and this for every point of its orbit. Thus for a TNO, if its ring falls totally within (without) the perturber's ring, i.e. if the condition $r_i < r_{\rm P9}$ ($r_i > r_{\rm P9}$) is satisfied over its complete orbit, the multipole expansion is reasonably adequate and compares favourably with the expansion adopted in spherical harmonics (Fig. 5).

This condition can be verified easily in concentric circular orbits. However, with particles and perturber on eccentric orbits, a particle's orbit has to be always within the perturber's periapse or always outside its apoapse for the multipolar description to converge. For eccentric TNOs of interest, the mass distribution of P9 is at times within their orbit, at others outside. The proper expansion in this case is the so-called Laplace expansion, with a switch in the ratio of radii reflecting the switch in hierarchy with respect to the central body. Orbit-averaged multipoles are unable to account for such a switch, whereas the orbit-averaged harmonics capture it automatically, by recovering the potential of the ring as a whole.

4.1 Sanity check: coplanar dynamics

To test the validity of our numerically generated potential, we recover Laplace equilibria in a configuration where P9, the inner quadrupole, and test particles of interest reside in the same plane. This setting was explored with various approaches to orbital averaging (Batygin & Brown 2016; Beust 2016; Saillenfest et al. 2017; Batygin et al. 2019). In our case, the Hamiltonian governing the particle's dynamics reduces to

$$\bar{\Phi}_{\rm planar} = -\frac{\Gamma}{3l_{\rm p}^3} + \bar{\Phi}_{\rm P9,planar}, \tag{19}$$

where the first term corresponds to the inner quadrupole, with Γ capturing the orbit-averaged forcing of the giant planets (equation A13), $l_{\rm p} = |\boldsymbol{j}| = \sqrt{1-e^2}$, and $\bar{\Phi}_{\rm P9,planar}$ denoting the planar restriction of the numerically computed 3D potential of P9 (equation A8), which can be written as

$$\begin{aligned}\bar{\Phi}_{\rm P9,planar}(a,e) = {} & \Upsilon_0(a,e) + \Upsilon_1(a,e)e\cos\Delta\varpi + \Upsilon_2(a,e)l_{\rm p}^2 \\ & + \Upsilon_5(a,e)e^2\cos^2\Delta\varpi + \Upsilon_6(a,e)l_{\rm p}^2 e\cos\Delta\varpi \\ & + \Upsilon_{10}(a,e)e^3\cos^3\Delta\varpi,\end{aligned} \tag{20}$$

where $\Delta\varpi$ is the particle's apsidal separation from the fixed apsidal orientation of P9, and the functions $\Upsilon_i(a,e)$ are defined in equations (A9).

We capture phase portraits for a sequence of particle semi-major axes in Fig. 6, then display Laplace equilibria for this coplanar configuration in Fig. 7. One family of stable (apsidally) aligned equilibria shows eccentricity growth with increasing semi-major axis. Another family of anti-aligned equilibria bifurcates with two stable branches beyond $a = 234$ au: one branch showing decreasing eccentricity with increasing a until it vanishes for $a > 290$ au, the other growing in eccentricity with increasing a, surviving beyond $a = 290$ au, reaching values as extreme as $e \approx 0.9$ by $a = 550$ au. Equilibria, their bifurcations, and the associated phase-space structure are largely analogous to those presented by Beust (2016) using numerical averaging of the full interaction potential. We further note agreement with trajectories of low-inclination TNOs presented in Li et al. (2018), with slight differences likely resulting from differences in P9 parameters.

In sum, using a rough and dirty shortcut to numerical averaging, we recovered key dynamical features in a weakly hierarchical problem, matching them to counterparts that were recovered with rather costly, nearly exact alternatives. At this stage, we hope we have given our reader enough confidence to follow us into the more treacherous triaxial landscape!

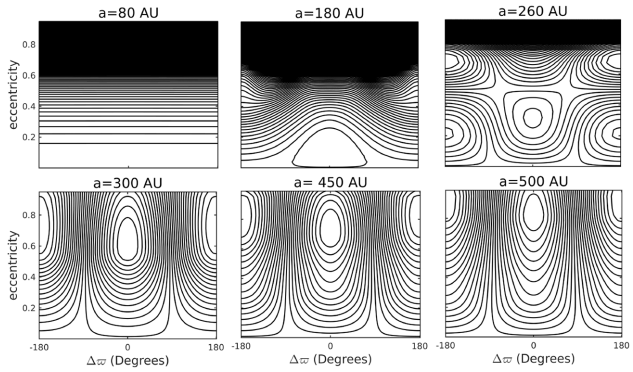

Figure 6. Phase portraits in $(\Delta\varpi, e)$ space corresponding to the planar Hamiltonian of equation (19) in which P9's potential is developed using the numerical harmonics toolbox. The chosen semi-major axis values cover the range over which the eTNOs are observed (see Table 1). For a relatively small semi-major axis of $a = 100$ au, the apsidal angle circulates. Beyond $a = 150$ au, TNOs can be captured in apsidally aligned or anti-aligned libration islands. A color version of this figure is available in the online journal.

Downloaded from https://academic.oup.com/mnras/article/507/4/6078/6362616 by CNRS user on 20 April 2023

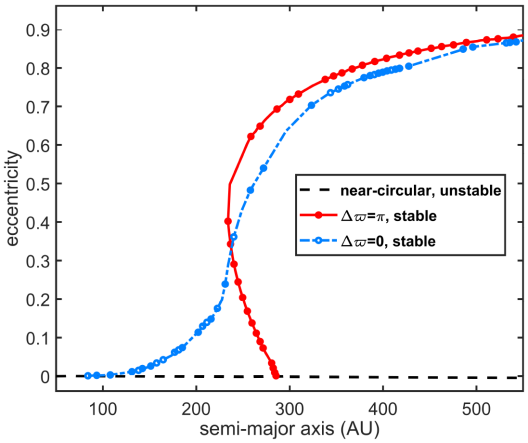

Figure 7. The eccentricity profile of stationary families of equilibria, both stable and unstable, apsidally aligned ($\Delta\varpi = 0$) and anti-aligned ($\Delta\varpi = \pi$) with the outer perturber, produced by solving the equation of motion (A14) over a range of semi-major axis a. The setting corresponds to the coplanar configuration where the giant planets, P9, and the test particles all live in the same plane. A color version of this figure is available in the online journal.

4.2 Moving on and out: fully spatial dynamics

To explore life beyond the coplanar setting, we introduce a finite tilt to the orbit of P9. We stick to the coplanar–coplanar equilibria of Section 2.1, thereby reducing the three-dimensional vectorial equations of motion (equations A10 and A11) into two coupled scalar equations for (e, i), with three input parameters: the particle's semi-major axis a, its apsidal orientation $\Delta\varpi$, and the mutual inclination between the perturbers Θ. For what follows, we shall pin our reference frame to the perturber's orbit, setting its inclination to zero and its argument of perisapse to $\pi/2$.

In Fig. 8, we present a sample of equilibria in (a, e) and (a, i) space for $\Theta = 10^\circ$. Pretty much as in the fully planar setting of Fig. 7, the stable, apsidally anti-aligned family persists when we tilt the perturber, though now starting beyond $a = 213$ au. It features an analogous eccentricity profile with semi-major axis, before two additional anti-aligned families bifurcate for $a > 391$ au: one stable and with larger eccentricity, the other unstable and with smaller eccentricity than the central stable family. The persisting anti-aligned family now acquires inclination with increasing semi-major axis, reaching $\simeq 50^\circ$ by 500 au, at which point the equilibrium eccentricity is close to 0.9. The bifurcating families emerge around an inclination $\simeq 25^\circ$, the unstable branch increasing in inclination towards 50°, while the inclination of the stable branch falls towards $\simeq 18^\circ$.

The aligned family, on the other hand, bifurcates into two distinct branches in the (a, e) plane, one stable and the other not, before disappearing altogether beyond $a > 342$ au. In the (a, i) plane, those two branches lie on a Laplace surface of sorts, which is stumped before hitting the outer plane. This is likely due to the inability of the giant planets to overcome the orbital precession of the aligned particles, due to the strong couple exerted by P9 in this outer region. Upon further testing, we find that a quadrupole of strength $\Gamma' = 2\Gamma$ suffices to maintain the highly eccentric aligned family, pretty much as in the planar setting, but laying it on a complete eccentric Laplace surface.

One can further note the presence of the retrograde and unstable Laplace structure in Fig. 8. This family starts in a polar configuration and turns increasingly retrograde with distance, to land eventually

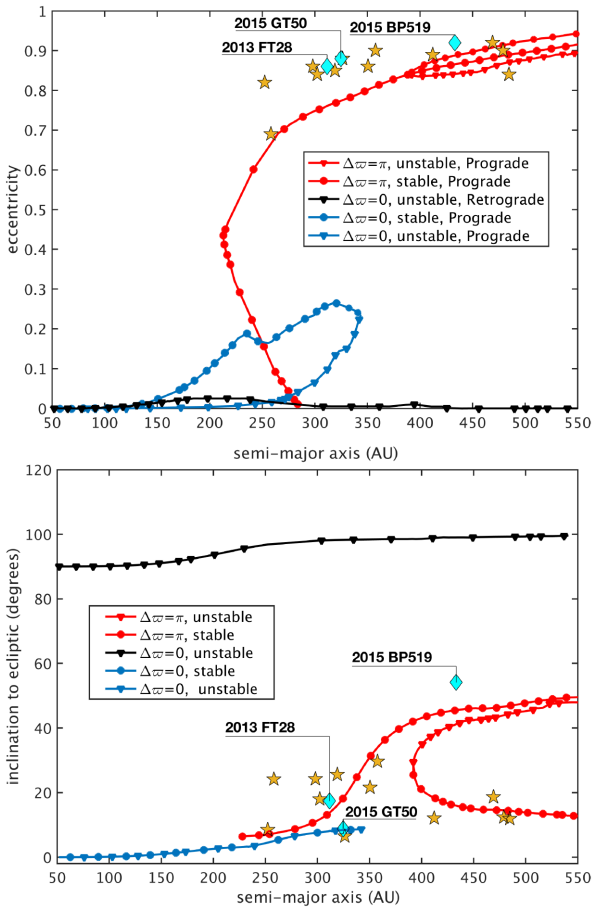

Figure 8. Equilibria of particles under the perturbation of the giant planets and the quasi-numerically computed effect of an inclined P9 (with $\Theta = 10^\circ$). *Top:* eccentricity profile of equilibria as a function of a. *Bottom:* inclination profile of equilibria as a function of a (inclinations are transformed here to the plane of the inner planets). Equilibria apsidally aligned (anti-aligned) with P9 are plotted in blue (red). Families of stable (unstable) equilibria are plotted in circles (triangles). Plotted on top of the equilibrium profile are the observed eTNOs of Table 1. A color version of this figure is available in the online journal.

around $\phi = \pi/2 + \Theta$, all the while maintaining a near-circular shape (near and never exactly so).

Overlaid over the equilibrium profiles in Fig. 8 are the elements of clustered TNOs (Table 1), the majority of which are apsidally anti-aligned with P9, with eccentricities and inclinations following families of stable Laplace equilibria quite closely. This is not the case for 'aligned' TNOs, the dynamics of which we discuss further below. We note that this equilibrium structure is robust to changes in Θ over a range of acceptable P9 inclinations: the eccentricity profile is maintained, with inclinations essentially following the mutual inclination.

4.2.1 *Poincaré sections locate Laplace in a sea of chaos*

To examine dynamics in the neighbourhood of Laplace equilibria, then of specific TNOs, further, we construct Poincaré sections on the (ω, e) plane with $\Omega = 0$. Restricting ourselves to crossings with $\dot{\Omega} < 0$, we follow orbits governed by equations (A10)–(A11) and with initial conditions selected from an energy hypersurface. Producing sections over an interesting range of energies at various representative values of a, we highlight key features.

Downloaded from https://academic.oup.com/mnras/article/507/4/6078/6362616 by CNRS user on 20 April 2023

Table 1. Orbital parameters of observed extreme TNOs of semi-major axis 250 au$<a<$ 650 au and pericentre distance beyond Neptune. Data collected from the IAU Minor Planet Center in 2020 July.

TNO	a (au)	e	i (°)	ω (°)	Ω (°)
2018 VM35	252.33	0.82	8.5	302.9	192.4
2012 VP113	258.27	0.69	24.1	293.5	90.7
2014 WB556	298.01	0.86	24.2	234.5	114.8
2014 SR349	302.23	0.84	17.9	340.9	34.8
2013 FT28	311.61	0.86	17.3	40.5	217.8
2004 VN112	318.97	0.85	25.6	326.8	66.0
2015 GT50	324.66	0.88	8.8	129.3	46.1
2013 SL102	326.18	0.88	6.5	265.4	94.6
2010 GB174	350.59	0.86	21.6	347.45	130.8
2013 RF98	357.63	0.90	29.6	311.6	67.6
2015 RX245	411.98	0.89	12.1	65.1	8.6
2015 BP519	433.17	0.92	54.1	348.2	135.0
2007 TG422	468.98	0.92	18.6	285.6	112.9
2013 RA109	478.90	0.90	12.4	262.8	104.7
SEDNA	484.52	0.84	11.9	311.5	144.3

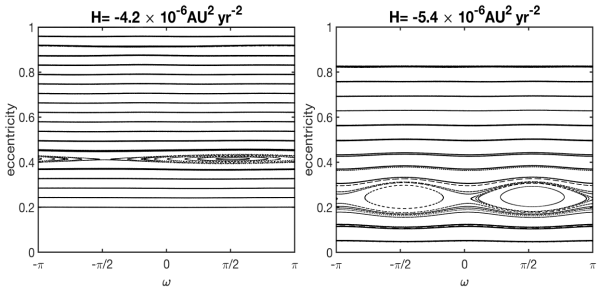

Figure 9. Poincaré sections for a test particle with $a = 60$ au, driven from the inside by the giant planets and from the outside by a hypothetical ninth planet. Initial conditions are selected on an energy hypersurface, trajectories sectioned in the (ω, e) plane for $\Omega = 0$, and crossings with $\dot{\Omega} < 0$. The left panel reveals fully regular motion over the whole range of eccentricity, with stable small-amplitude librations in eccentricity around $e \approx 0.4$ and $\omega = \pi/2$ and an unstable fixed point around $\omega = -\pi/2$. In the right panel, we explore dynamics at a lower energy, with stable librations around $\pm\pi/2$ and the smaller eccentricity of $\approx$0.2. Fixed points correspond to period orbits with inclination around 64°. A color version of this figure is available in the online journal.

(i) $a = 60$ au (Fig. 9): we start with a rather tame case at a relatively small semi-major axis where a TNO's dynamics is largely dominated by the inner quarupole, with near-conservation of the vertical angular momentum $\sqrt{1-e^2}\cos i$. Dynamics on the section is fully regular, with a persistent libration zone around $\omega = \pi/2$ and a bifurcation at $\omega = -\pi/2$ with decreasing energy. Relative equilibria have inclinations $\approx$64°, and they correspond to periodic orbits with finite $\dot{\Omega}$, as opposed to $\dot{\Omega} = 0$ in the case of Laplace equilibria. The behaviour is consistent with outer Kozai–Lidov dynamics associated with the inner quadrupole, dynamics which will be gradually encroached upon as we progress to larger semi-major axes (Saillenfest et al. 2017).

(ii) $a = 258$ au (Fig. 10): the interplay between the inner and external perturbers is now manifest, with chaos emerging around libration zones and chains of resonant islands embedded within them. At $H = -5.3 \times 10^{-6}$ au^2 yr^{-2}, we follow dynamics with the secular energy of 2012 VP113. The aligned libration zone is encroached upon with chaotic trajectories, while the anti-aligned resonance persists.

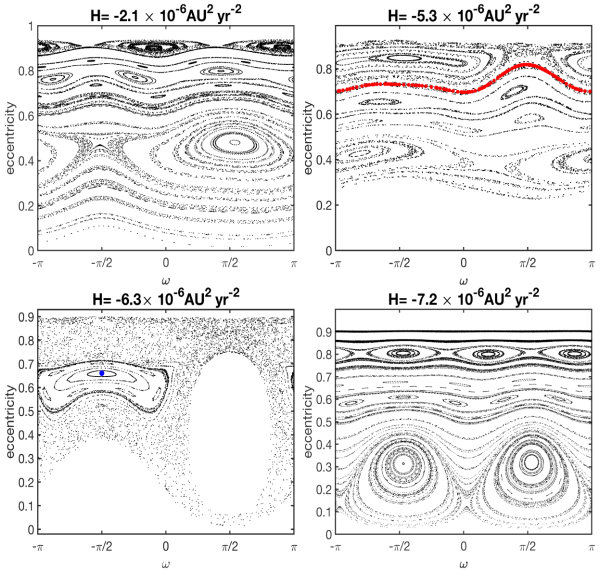

Figure 10. Same as Fig. 9, but at $a = 258$ au corresponding to TNO 2012 VP113. We section at energies straddling the energy of this TNO, passing by the energy of the stable anti-aligned Laplace equilibrium at this semi-major axis. The top right panel reveals a typical mixed phase space with quasi-periodic motion, tori broken into islands, chaotic zones confined around separatrices, etc. At the lower secular energy of 2012 VP113 in the top right panel, a well-defined libration zone emerges around anti-aligned orientations, with the TNO's trajectory (shown in red) hugging it as it circulates between the stable anti-aligned and the unstable aligned fixed points. At a lower energy still, we come across the apsidally anti-aligned Laplace equilibrium at this semi-major axis, which is marked with a blue dot in the lower left panel. The libration zone associated with this stable equilibrium is embedded in an extended chaotic zone, which connects its neighbourhood with that of a Kozai–Lidov island to its right. The lower right panel samples the lowest energy at this semi-major axis, revealing a fully regularized phase space with stable aligned and anti-aligned islands now around $e \approx 0.3$. A color version of this figure is available in the online journal.

Below this libration zone, we plot in red the torus 'associated' with this TNO (which is known to be stable: Batygin et al. 2019). We observe circulation from anti-aligned to aligned configurations (occurring over a $\sim$100-Myr time-scale), which, when taking the model and initial conditions for granted, suggests several changes of apsidal orientation over the age of the Solar system, for this and other TNOs, potentially explaining the opposite apsidal orientation of the likes of 2013 FT28, despite having elements that are consistent with anti-aligned high eccentricity Laplace equilibria. The phase-space shows interplay between Laplace equilibrium islands and islands harbouring Kozai–Lidov-like cycling, connected through a sea of chaos signaling resonant interactions induced by the outer perturber.

(iii) $a = 302$ au (Fig. 11): the stable high-eccentricity anti-aligned equilibrium is tucked within a surviving libration island, which is further embedded in an extended chaotic zone. Shown in the lower left panel is the trajectory of 2014 SR349, describing quasi-periodic motion within the apsidally anti-aligned libration island around a stable periodic centre. At the higher energy of $H = -8.9 \times 10^{-7}$ au^2 yr^{-2}, we code further for inclination, revealing how trajectories can transition from aligned, near-circular orbits at moderate inclination (40°) to anti-aligned, highly eccentric (0.8) and fairly inclined orbits (80°). One can then envisage a scenario of decreasing secular energy (at constant a), whereby a TNO would transition from the upper to the lower left panel of Fig. 11, from a

Downloaded from https://academic.oup.com/mnras/article/507/4/6078/6362616 by CNRS user on 20 April 2023

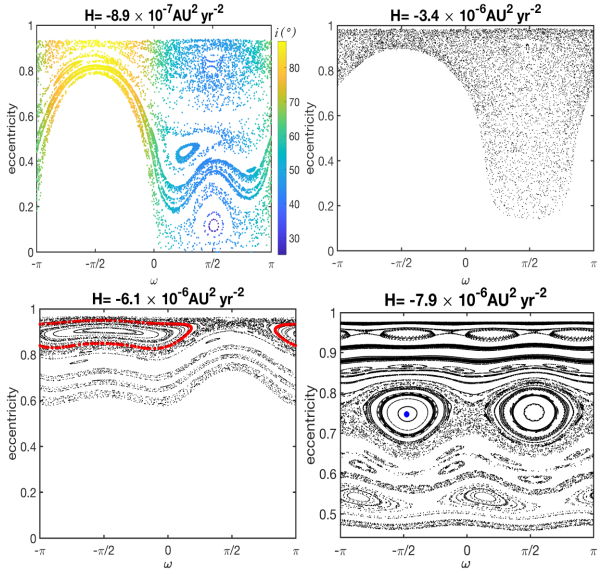

Figure 11. Same as Fig. 9 but at $a = 302$ au, corresponding to 2014 SR349. The Poincaré section in the top left panel is colour-coded to show inclination variations of the crossings, suggesting possible transitions from a moderate-inclination and low-eccentricity apsidally aligned zone to high-inclination and high-eccentricity apsidally anti-aligned zone (see text). Proceeding with the lower energy of the top right panel, we follow the disappearance of islands at low and high eccentricity, as a broad chaotic zone occupies the allowable phase space. The section in the lower left panel is computed at the secular energy of the TNO in question. The crossings of its trajectory are plotted in red, revealing quasi-periodic motion around the anti-aligned island. The section in the lower right panel is computed at the secular energy of the stable anti-aligned Laplace equilibrium, which is shown in blue at the centre of the libration zone. A color version of this figure is available in the online journal.

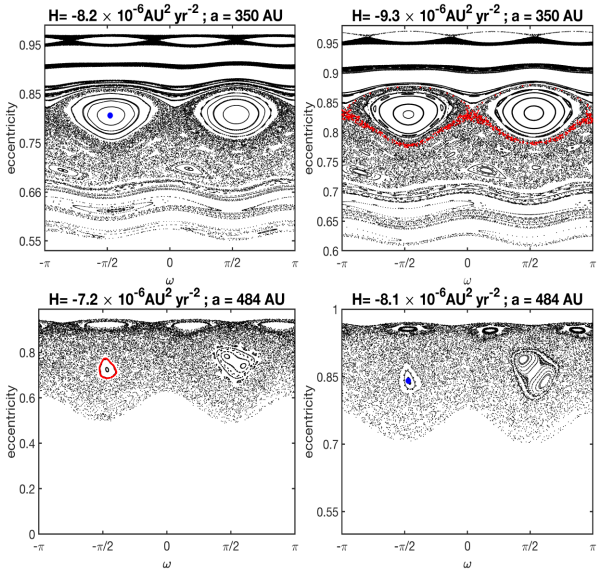

Figure 12. Same as Fig. 9 but at $a = 350$ au in the top panels corresponding to 2014 GB174, and at $a = 484$ au in the bottom panels corresponding to the TNO SEDNA. We section at energies corresponding to the TNOs current trajectories and to stable anti-aligned Laplace equilibria. The trajectory of 2014 GB174 in the top right panel traces chaotic transitions between apsidal alignment and anti-alignment, spending most of its time below the libration islands. Decreasing the energy and moving to the left panel, the phase-space structure is largely intact as we locate the Laplace equilibrium centring the anti-aligned libration island. Moving to $a = 484$ au, SEDNA's trajectory inhabits a torus confined within the – now very narrow – anti-aligned libration zone. A slight increase in energy reveals the Laplace equilibrium marked in blue in the right panel. Both sections feature chaotic trajectories occupying the larger area of the restricted phase space. A color version of this figure is available in the online journal.

chaotic trajectory at high eccentricity and inclination to a trapped torus at lower energy and similar orbital architecture. Protoplanetary disc dissipation and/or planetary migration can bring about such a decrease, and with it the trapping of TNOs around the desired eccentric Laplace configuration.

(iv) $a = 350$ au (Fig. 12, top panels): we display on the left the stable anti-aligned eccentric Laplace equilibrium embedded within a phase-space structure similar to that around equilibrium for $a = 302$ au. On the right, the section is computed at the estimated secular energy of 2010 GB174. Its trajectory appears to circulate chaotically between aligned and anti-aligned orientations, but still within a relatively narrow chaotic zone, straddling the separatrices, as it hugs the surviving libration zones.

(v) $a = 484$ au (Fig. 12, bottom panels): in the left panel, we display the Poincaré section at the estimated secular energy of SEDNA. SEDNA's trajectory is shown in red, a regular torus that is strictly confined within the anti-aligned libration zone. At this semi-major axis, the main anti-aligned family has reached moderate ecliptic inclinations ($i_E \approx 43°$). SEDNA's secular energy is actually quite close to the energy of the Laplace equilibrium at that semi-major axis, which is marked on the bottom right panel. Note the narrow allowable range in (high) eccentricity, which is largely occupied by chaos, barring a narrow region of quasi-periodic librations, which appear to shelter SEDNA, as well as the stable highly eccentric and moderately inclined Laplace equilibrium. Any scenario addressing the clustering of TNOs must explain their transport and confinement around similar high eccentricity and moderately large inclinations.

We located eccentric Laplace equilibria within the full phase space available at their, and neighbouring, energies. We focused on semi-major axes associated with observed TNOs and featured their secular dynamics, taking initial conditions as indicators of secular orbital elements within our model. Some appeared to be caught in finite-amplitude stable librations, others to be circulating, on a stable torus in some cases and around a compact chaotic zone in others. We examined the expected interplay between Laplace and Kozai–Lidov dynamics, as test particles with increasing a move from being dominated by the inner perturber to being strongly affected by the outer perturber, with an intermediate zone in between. Though they might appear indistinguishable in the (ω, e) phase space, Laplace and Kozai–Lidov libration zones surround equilibria and periodic orbits respectively and are connected by transfer orbits transporting particles from near-zero eccentricity and small to moderate inclination around Kozai–Lidov cycling to the high-eccentricity and inclination neighbourhood of eccentric Laplace equilibria. Such transfer becomes more pronounced with increasing a, as aligned and anti-aligned Laplace equilibria increase in inclination, while the inclination of relative Kozai–Lidov equilibria decreases monotonically with a TNO's semi-major axis. There is much to explore regarding this geography, with evident implications for the shaping of TNO orbits by the envisaged P9, but more generally for the sculpting of debris discs by binary companions.

Downloaded from https://academic.oup.com/mnras/article/507/4/6078/6362616 by CNRS user on 20 April 2023

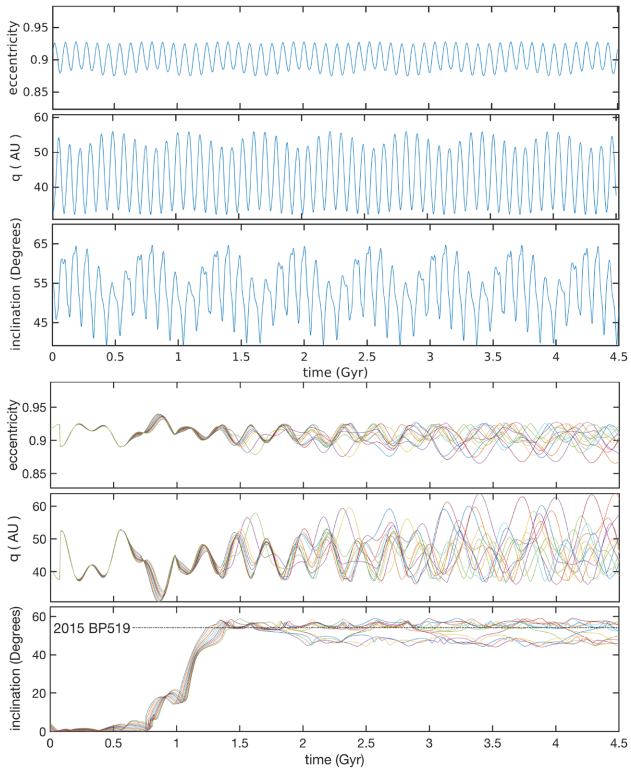

Figure 13. Numerical integration of the equations of motion showing the evolution of the orbital elements of clones of 2015 BP519 under the influence of the giant planets and the putative P9. Top: initial conditions are exactly the elements of the TNO in Table 1. Bottom: we changed the initial inclination to start around the ecliptic ($0 \leq i_0 \leq 5^\circ$) and the apsidal orientation to start aligned with the outer planet. A color version of this figure is available in the online journal.

4.2.2 *Case study: 2015 BP519*

Among the TNOs in Table 1, Object 2015 BP519 displays curious enough behaviour to be featured in this context, as it was in other contexts. Nicknamed *Caju*, it has the highest inclination above the ecliptic ($\sim 54^\circ$), and the closest approach to Neptune ($q \simeq 35.2$ au). Becker et al. (2018) asked two questions concerning the origin and dynamical evolution of this object: (i) can it attain its current configuration starting close to the invariable plane, and (ii) will it maintain its current configuration in the future? They answer both questions in the affirmative using *N*-body simulations. We revisit them both within our secular framework.

In the top panel of Fig. 13, we follow the object over the age of the Solar system when initiated around its current orbit. The eccentricity shows small-amplitude oscillations ($\Delta e \simeq \pm 0.025$) around $e = 0.9$. The inclination behaviour is quasi-periodic around its current value, but with relatively large-amplitude oscillations, $i = 52.5^\circ \pm 12^\circ$. Pericentre distance varies between $q = 56$ au and $q = 32.7$ au. Secular *Caju* appears trapped in and around its current orbital configuration. In the left panel of Fig. 14, we constructed the corresponding surface of section in (ω, e) space. At *Caju*'s energy, much of phase space is inaccessible, with section-crossing trajectories confined to a narrow range in eccentricity, above $e = 0.78$. This region is almost completely filled by chaotic trajectories, except for two evident libration islands around $\omega = \pm\pi/2$. In red, we trace *Caju*'s trajectory, which appears to evolve quasi-periodically within the anti-aligned libration zone.

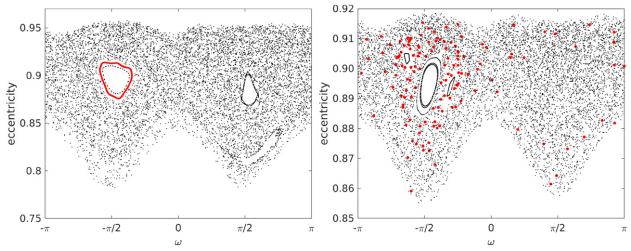

Figure 14. Same as Fig. 9 but at the semi-major axis $a = 434$ au corresponding to 2015 BP519. The first panel is the section computed at the value of the secular Hamiltonian of this TNO corresponding to its orbital elements as observed and recorded in Table 1. Its trajectory crossings on the section in red appear to occupy the anti-aligned libration zone. The second panel corresponds to the energy computed for the TNO starting in the ecliptic and around apsidal alignment with P9. A color version of this figure is available in the online journal.

We then track the evolution of 12 hypothetical *Cajus*, all sharing the same current eccentricity, but with inclinations reset closer to the ecliptic (and picked randomly in the range $0 \leq i_0 \leq 5^\circ$) and orientation aligned with the outer perturber. As seen in Fig. 13, all particles follow nearly identical low-inclination trajectories until about $t = 0.86$ Gyr, when they become unstuck from the ecliptic, with inclinations experiencing a relatively fast period of growth to around the current value. Beyond this point, trajectories start diffusing away from each other and evolving chaotically over a bounded range of fairly high eccentricity and inclination. The surface of section at a typical clone energy (Fig. 14, right panel) reveals a connected chaotic zone between aligned and anti-aligned orientation, between low inclination and high inclination, and consistently high eccentricity. A sample clone hops around the aligned zone for less than a billion years, then eventually tunnels to the anti-aligned zone and is stuck diffusing chaotically around a surviving anti-aligned island.[2] The sharp increase in inclination noted earlier correlates quite neatly with the transition from aligned to anti-aligned chaotic zones. The evolution was extended for twice the displayed duration, with clones remaining trapped around the anti-aligned high-inclination zone, with no signs of transition back to aligned, near-ecliptic orientations.

We discussed how processes that bring about a decrease in secular energy can leave 2014 SR349 trapped in its orbit, having migrated through its chaotic phase space from an initially circular and moderately inclined orbit. The same process can leave *Caju* trapped in quasi-periodic oscillations, but requires it to start life near the ecliptic and with a fairly large eccentricity. It remains to be seen whether evolutionary processes can, when coupled to rich secular dynamical evolution, bring about anti-aligned or aligned clustering at high eccentricity and inclination, with TNOs starting around the ecliptic with relatively small eccentricity.

5 DISCUSSION

Before concluding, we offer some remarks putting our work in context, drawing implications, and reporting on extensions.

[2] As evident in Fig. 13, both regular and chaotic dynamical evolution of Caju and its clones lead to close encounters with Neptune, forcing diffusion in its semi-major axis, which is otherwise maintained constant in our secular analysis. Aside from highlighting this limitation here and in other sections, we do not take measures to correct for this and related effects. The simplest such measures are expected to be involved enough to deserve a separate treatment.

Downloaded from https://academic.oup.com/mnras/article/507/4/6078/6362616 by CNRS user on 20 April 2023

(i) *On inclined equilibria.* We explored eccentric inclined equilibria with TNOs in mind, but our results may very well be relevant to exoplanetary systems. In that context, variations in the inner quadrupole (Spalding & Batygin 2016; Spalding, Marx & Batygin 2018), then giant planets residing in wide inclined orbits (Pu & Lai 2018) have been shown to excite mutual inclination in multiplanet systems. We combined both effects and showed how they annihilate on eccentric and inclined orbits on the eccentric Laplace surface. The fictitious system of Section 3.2 is not unlike Kepler-108 (Rowe et al. 2014), with an inner planet, Kepler-108 b, serving as the inner quadrupole, and the stellar companion, Kepler-108 A, providing the inclined and eccentric wide perturber, both torquing the planet between them, Kepler-108 c. The observed mutual inclination of $24^{+11\circ}_{-8}$ (Mills & Fabrycky 2017) is consistent with the results reported in Figs 2 and 3, though further investigation is required due to the proximity and comparable masses of the planets.

(ii) *On P9 alternatives.* Sefilian & Touma (2019) argued that a moderately eccentric ($e \approx 0.2$) disc extending between 40 and 750 au with a mass of $10\,M_\oplus$ can, together with the giant planets, shepherd TNOs into coplanar apse-aligned configurations. They further suggested that the combined action of such a disc, the giant planets, and a scattered inclined planetary embryo (outcome of the simulation in Silsbee & Tremaine 2018) might be enough to maintain TNOs in inclined apse-aligned configurations. This of course smells like the eccentric, inclined spatially frozen Laplace equilibria of our theory. Our preliminary explorations of this setting involved generalizing the modal structure from one ring describing P9 to N rings describing a self-gravitating precessing debris disc. Combining the action of this disc with the giant planets and an inclined planetary embryo as small as Mars, we could recover families of eccentric and moderately inclined equilibria that match the orbital trends of the observed TNOs without the need for a massive outer planet.

(iii) *P9 and TNO clustering.* In this work, our intention is not to engage critically with the P9 hypothesis. Rather, we simply argue that eccentric inclined Laplace equilibria in the combined field of the gaseous giants and a putative P9 are those desired frozen orbits around which the TNOs can be clustered in librating apse-aligned configurations. We argue along those lines and proceed to solve for this skeletal structure, then map the chaotic secular phase space within which it is embedded.

We showed how the planar structure of equilibria is smoothly transported into an off-plane structure upon tilting the orbit of P9. Libration islands around equilibria could harbour apsidal anti-aligned clustering, as shown specifically for 2014 SR349, 2015 BP519, and SEDNA. The apsidal orientation of the likes of 2013 FT28 and 2015 KG163 can be further explained by the emergence of a highly eccentric aligned family or trajectories surfing both apsidal areas of the Poincaré sections.

Furthermore, one notes that clustering obtains through confinement of trajectories to compact chaotic zones in phase space, for a broad range in energy (similar behaviour was reported in Saillenfest et al. 2017). Such confinement is often accompanied by circulation between anti-aligned and aligned configurations, typically over a 100-Myr time-scale. Thus, it should not be surprising to find objects with the high eccentricity and inclination of an anti-aligned Laplace equilibrium, spatially aligned with the outer perturber's periapse. The more pressing question for any similar such scenario for TNO clustering is how to get them trapped out there in the first place!

We leave it to P9 enthusiasts to consider and assess evolutionary scenarios over the (secular) dynamical landscape. This said, we have highlighted promising cases where chaotic exchange orbits between Kozai–Lidov and Laplace-like regimes can provide a vehicle for transporting TNOs close to high-eccentricity/high-inclination Laplace equilibria. A slight tip in energy can leave that same object trapped around its neighbouring Laplace equilibrium.

Our secular formalism does not allow for semi-major axis diffusion, which seems tolerable given how the semi-major axis time series of most of the objects presented in Batygin et al. (2019) showed no marked diffusion. It further excludes confinement due to mean-motion resonances with the gaseous planets, or disruption of secular equilibria by those same resonances. Much remains to be done on this front, and, for a start, it would be interesting to explore perturbations of idealized secular equilibria by terms in the disturbing function which are of second order in the masses.

(iv) *Equilibria and slow nodal regression.* Fixing a perturber's orientation reveals dynamics for a specific configuration, at a particular point in time, whereas we know that both outer and inner perturbers precess – slowly, but they precess none the less. Indeed, a P9-like object is expected to precess with a 10 billion year time-scale and force the inner quadrupole into precession over a 100 billion year time-scale. Contrast this with the expected secular dynamical time-scales of TNOs (two to three orders of magnitude faster, with typically a 100-Myr precession period) and you can see why we are fully justified in working in the adiabatic limit (Arnol'd 2013). In that limit, equilibria are expected to remain close to equilibria and quasi-periodic motion to deform into quasi-periodic motion, with an adiabatically invariant action, suitably defined over the surface of section. Those expectations were confirmed in extensive simulations exploring dynamics in a sequence of Hamiltonians corresponding to perturbers that are frozen in a sequence of relative orientations. Libration zones around stable Laplace equilibria were seen to oscillate as they deform adiabatically with the circulating quadrupole. This was the case over a range of semi-major axes, suggesting that equilibrium families, rather than being tuned to the particular orientation of Fig. 8, are largely preserved as they deform adiabatically, reversibly, with quasi-periodic adiabatic changes in the perturbers. These are preliminary results to be sure, and deserving of further exploration, but encouraging none the less.

(v) *On weakly hierarchical systems.* Our method for dealing with such systems has much promise and deserves to be further confronted with costlier though more accurate numerical double averaging (Beust 2016; Batygin & Morbidelli 2017). The astute reader may wonder about the structural stability of the equilibria we recovered with this approach, when one increases the order of harmonics included in the potential of the outer perturber. We wondered the same and learned that, having passed the convergence test, harmonics of order higher than the third considered in our work produced an almost identical skeleton of equilibria, confirming the robustness of our results and their reliability as a foundation for further studies. That same reader may worry further about particles within a semi-major axis and eccentricity range suitable for hierarchy to be violated not only for the outer perturber (which we focused on here) but also for the inner one (which we invariably modelled as a quadrupole). While equilibria of interest to us here and librations around them do not face this complication, some of the trajectories displayed on surfaces of sections do. Such pathologies can be efficiently handled by working out the orbit-averaged spherical harmonic expansion of inner and outer perturbers (of arbitrary eccentricity), thus allowing for global mapping of secular motion (albeit with softened crossings of perturbers). Before concluding this segment, it is perhaps worth emphasizing that the method we presented is ideally suited for fixed or uniformly precessing configurations (irrespective of the number of perturbers, as was demonstrated recently in Sefilian & Touma 2019). Of course, the method of choice to capture fully

Downloaded from https://academic.oup.com/mnras/article/507/4/6078/6362616 by CNRS user on 20 April 2023

the secular test particle evolution coupled to dynamically evolving (inner and/or outer) perturbers is the softened Gauss algorithm (Touma, Tremaine & Kazandjian 2009), which we hope to deploy on generalized Laplace dynamics in the near future.

6 CONCLUSIONS

We examined the orbital architecture of test particles under the combined effect of an inner and an outer perturber residing on an inclined and eccentric orbit. Classically, inner and outer perturbers are included up to quadrupolar level, and the problem reduces to finding stationary test particle orbits on which the secular perturbation of the combined quadrupoles vanishes (Tremaine et al. 2009). Critical to this story is the so-called Laplace surface. Traced by a distinguished family of circular Laplace equilibria, this warped surface coincides with the plane of the inner perturber close in and transitions to the plane of the outer perturber at large distances. It has played a fundamental role in the understanding of planetary satellites, our Moon included, and has experienced a dramatic revival as theorists grapple with an influx of complex hierarchical architectures, from the plethora of exoplanetary systems on one scale to stellar black hole nuclei on another.

Our work generalizes the already productive generalization of Tremaine et al. (2009) by including higher order, symmetry-breaking perturbations from an eccentric outer perturber, all the while following the authors' lead in exploring equilibria in arbitrary architectures. Our generalization is meant to bring Laplace surface dynamics closer in touch with the following: exoplanetary architectures with highly eccentric wide binary companions; satellite dynamics around planets undergoing eccentric Kozai–Lidov cycling; secular dynamics of accretion discs and stellar clusters with an eccentric binary black hole; and/or debris disc architecture with gaseous giants tucked in and a massive eccentric perturber, be it an outer planet, the disc itself, or both.

Focusing on circular equilibria, it is perhaps not surprising to learn that the inclusion of an outer octupole shatters the classical Laplace surface, leaving an eccentric Laplace surface on its ruins. This surface is parametrized with eccentric, inclined, equilibrium orbits, evolving in orientation in a manner analogous to their classical counterparts, with eccentricity increasing as they approach the outer perturber. Interestingly enough, this surface is accompanied by the bifurcation of stable, retrograde, and highly eccentric families of equilibria.

We highlight the significance of those novel equilibria for various current astrophysical settings. In an exoplanetary system, where the inner quadrupole is provided by a compact coplanar system and the outer octupole by an inclined and eccentric outer massive planet or a stellar companion, the eccentric Laplace surface may help explain observed mutual inclinations and eccentricities of architecturally complex systems like Kepler-108 and Kepler 419 (Dawson et al. 2014; Rowe et al. 2014).

Closer to home, it was natural to examine the frozen orbits of our generalized Laplace equilibria as natural parking (phase) space for TNOs under the combined gravitational perturbations of the outer planets and a hypothetical ninth planet (Trujillo & Sheppard 2014; Batygin et al. 2019). As the setting is weakly hierarchical, trusted multipole expansions are hopelessly divergent over a wide range of relevant semi-major axes. Previous studies dealt with this problem through costly 'exact' numerical averaging of the Hamiltonian (Beust 2016; Saillenfest et al. 2017). We overcame this hurdle with a reasonably efficient and accurate fix, capturing the averaged potential of an outer perturber (thought of as a Gaussian ring of arbitrary eccentricity and orientation à la Touma et al. 2009) through spherical harmonics, which are then averaged over an arbitrary test particle orbit.

Suspending concerns about observational bias (Brown 2017; Shankman et al. 2017; Napier et al. 2021), we use our tested and versatile toolbox to show how families of eccentric, inclined, and stable Laplace equilibria maintained by a fiducial ninth planet are strongly correlated with the phase-space distribution of the TNOs that planet is expected to shepherd. We thus confirmed our hunch on eccentric, high-inclination Laplace clustering, further providing modellers with a skeletal structure of secular equilibria around which to elaborate variations with non-secular effects, should they so desire.

Equilibria were further situated within the broader phase space as we mapped global dynamics with suitably constructed Poincaré sections, at TNO semi-major axes and with energies close to our best estimate of TNO secular energy. Stable equilibria emerged at the centres of libration zones, themselves potential trapping zones for clustered TNOs. Chaotic dynamics was shown to engulf the available phase-space volume with increasing TNO semi-major axis. We gave further evidence of stickiness within chaos, providing long-term confinement of TNOs, diffusive though it may be. With global structure in hand, we explored the evolution of the highly inclined TNO 2015 BP519. Using current conditions, we reveal its confinement as it librates around the neighbouring Laplace equilibrium; then, allowing it to start life closer to the ecliptic, we showed how (in agreement with Becker et al. 2018) it can evolve and then stick and diffuse around its current inclination. We further revealed the coming together of two secular dynamical features, Laplace and Kozai–Lidov, with Laplace equilibria growing in inclination as we approach the outer perturber and the Kozai–Lidov zone decaying to settle into low-inclination regimes. This sequence of events, and the geometry that underlies it, is further shown to be robust to slow nodal precession of the inner quadrupole, an adiabatic regime in which equilibria and associated islands survive as they undergo slow periodic shifts with the periodically varying orientation of perturbers (inner and outer alike).

In our discussion, we highlight various implications and variations. In particular, and building on a proposition of Sefilian & Touma (2019), we reported preliminary results on how an extended and moderately eccentric precessing debris disc can join forces with an inclined planetary embryo, as puny as Mars, to self-consistently generate a structure of equilibria that also matches the trend of the orbital parameter of the TNOs, without the need for an extra massive planet.

So where does all this leave us? Well, the last major generalization of Laplace's work ushered in a stream of applications, mainly to extrasolar settings (Muñoz & Lai 2015; Zanazzi & Lai 2016), but also to scenarios of lunar formation, which argue for an initially steeply oblique and fast-spinning Earth (Ćuk et al. 2016, 2021; Tian & Wisdom 2020). We can foresee the same for our renewed focus on the foundations of the Laplace surface itself and for the rich structure of equilibria we have identified, with applications ranging from manmade satellites to exomoons around planets on Kozai–Lidov cycles, then debris discs with enclosed planets, the whole perturbed by a wide eccentric binary. A key missing ingredient in our story, one that was alluded to in discussion, concerns evolutionary processes (protoplanetary disc dissipation, instabilities in multiplanet systems, planetary migration, disc relaxation, and potential instabilities encountered on the way), which can then allow for dramatic events over the phase-space structure of our work: loss of stability through bifurcations, capture and evolution along a specific family of equilibria, transition between Kozai–Lidov and Laplace regimes, and the implication of those phenomena for the carving of distributions of particles, including the emergence of clustering, should that be

Downloaded from https://academic.oup.com/mnras/article/507/4/6078/6362616 by CNRS user on 20 April 2023

of interest! Within the octupolar limit, we have barely managed to map out one class of equilibria, the so called coplanar–coplanar variety, and draw out its consequences for various astrophysical applications. Considered in full generality, our dynamical systems sustains additional, orthogonal, equilibrium geometries which are worth mapping in full detail, again with various potential applications in mind (refer to Tremaine et al. 2009 for further discussion). Finally, having developed machinery for the harmonics of a single ring, it would be natural to deploy it on a distribution of such rings, perhaps one representing the lopsided thermodynamic equilibria of self-gravitating secular discs in the presence of an inner quadrupolar perturber, be it a a supermassive black hole binary, a planet, or a system of such planets.

ACKNOWLEDGEMENTS

This manuscript grew out of MF's master's thesis work in the Department of Physics at the American University of Beirut (AUB). As such, it has benefited from invaluable discussion with thesis committee members Leonid Klushin and Scott Tremaine, the support of students and staff in the Department, and vital access to AUB's High Performance Computing facility. MF further thanks Mher Kazandijian and Antranik Sefilian for assistance with the modal analysis toolbox. We received valuable feedback from two generous readers: the referee Konstantin Batygin, whose enthusiastic report boosted our resolve to explore astrophysical implications of our work further; and Melaine Sallienfest, whose questions and remarks on an earlier draft led to clarifications in the present one.

DATA AVAILABILITY

The data underlying this article pertaining to the orbital parameters of trans-Neptunian objects are collected from the IAU Minor Planet Center at https://www.minorplanetcenter.net/iau/mpc.html.

REFERENCES

Allan R., Cook G., 1964, Proc. R. Soc. London Ser. A, Mathematical and Physical Sciences, 280, 97
Arnol'd V. I., 2013, Mathematical methods of classical mechanics, Vol. 60. Springer Science & Business Media, Berlin
Batygin K., Brown M. E., 2016, AJ, 151, 22
Batygin K., Morbidelli A., 2017, AJ, 154, 229
Batygin K., Adams F. C., Brown M. E., Becker J. C., 2019, Phys. Rep., 805, 1
Becker J. et al., 2018, AJ, 156, 81
Beust H., 2016, A&A, 590, L2
Brown M. E., 2017, AJ, 154, 65
Charnoz S., Canup R. M., Crida A., Dones L., 2018, The Origin of Planetary Ring Systems. Cambridge Univ. Press, Cambridge, p. 517
Correia A. C., Laskar J., Farago F., Boué G., 2011, Cel. Mech. Dyn. Astron., 111, 105
Dawson R. I. et al., 2014, ApJ, 791, 89
Fienga A., Di Ruscio A., Bernus L., Deram P., Durante D., Laskar J., Iess L., 2020, A&A, 640, A6
Hamers A. S., 2020, MNRAS, 494, 5492
Holman M. J., Payne M. J., 2016, AJ, 152, 94
Laplace P.-S., 1805, Mecanique Celeste, Vol. 4. Courcier, Paris
Li G., Hadden S., Payne M., Holman M. J., 2018, AJ, 156, 263
Malhotra R., Volk K., Wang X., 2016, ApJ, 824, L22
Migaszewski C., Goździewski K., 2008, MNRAS, 388, 789
Migaszewski C., Goździewski K., 2009, MNRAS, 395, 1777
Mills S. M., Fabrycky D. C., 2017, AJ, 153, 45
Muñoz D. J., Lai D., 2015, Proc. Natl Acad. Sci., 112, 9264
Napier K. et al., 2021, Planetary Sci. J., 2, 59
Pu B., Lai D., 2018, MNRAS, 478, 197
Rosengren A. J., Scheeres D. J., 2014, ApJ, 786, 45
Rowe J. F. et al., 2014, ApJ, 784, 45
Saillenfest M., Fouchard M., Tommei G., Valsecchi G. B., 2017, Cel. Mech. Dyn. Astron., 129, 329
Sefilian A. A., Touma J. R., 2019, AJ, 157, 59
Shankman C. et al., 2017, AJ, 154, 50
Silsbee K., Tremaine S., 2018, AJ, 155, 75
Spalding C., Batygin K., 2016, ApJ, 830, 5
Spalding C., Marx N. W., Batygin K., 2018, AJ, 155, 167
Tamayo D., Burns J. A., Hamilton D. P., Nicholson P. D., 2013, AJ, 145, 54
Tian Z., Wisdom J., 2020, Proc. Natl Acad. Sci., 117, 15460
Touma J., Tremaine S., Kazandjian M., 2009, MNRAS, 394, 1085
Tremaine S., Touma J., Namouni F., 2009, AJ, 137, 3706
Trujillo C. A., Sheppard S. S., 2014, Nature, 507, 471
Zanazzi J., Lai D., 2016, MNRAS, 464, 3945
Ćuk M., Hamilton D. P., Lock S. J., Stewart S. T., 2016, Nature, 539, 402
Ćuk M., Lock S. J., Stewart S. T., Hamilton D. P., 2021, Planetary Sci. J., 2, 147

APPENDIX A: ORBIT-AVERAGED POTENTIAL OF THE P9 GAUSSIAN RING

The gravitational potential of the Gaussian ring associated with P9 is computed numerically over a three-dimensional grid, then expanded in spherical harmonics. Allowing for the dominant non-axisymmetric modes (shown in Fig. A1), together with the axisymmetric contribution of course, we end up with

$$\begin{aligned}\Phi_{\rm P9}(r,\theta,\phi) &= A_0^0 Y_0^0 \cos\psi_0^0 + A_1^1 Y_1^1 \cos\psi_1^1 + A_2^0 Y_2^0 \cos\psi_2^0 \\ &\quad + A_2^2 Y_2^2 \cos\psi_2^2 + A_3^1 Y_3^1 \cos\psi_3^1 + A_3^3 Y_3^3 \cos\psi_3^3 \\ &= -\frac{1}{\sqrt{4\pi}} A_0^0 - \sqrt{\frac{3}{8\pi}} \sin\theta\cos\phi A_1^1 + \sqrt{\frac{5}{16\pi}} \\ &\quad \times \left(3\cos^2\theta - 1\right) A_2^0 + \sqrt{\frac{15}{32\pi}} \sin^2\theta \cos 2\phi \cos\psi_2^2 A_2^2 \\ &\quad + \sqrt{\frac{35}{64\pi}} \sin^3\theta \cos 3\phi \cos\psi_3^3 A_3^3 - \sqrt{\frac{21}{64\pi}} \sin\theta \\ &\quad \times \left(5\cos^2\theta - 1\right) \cos\phi \cos\psi_3^1 A_3^1. \end{aligned} \tag{A1}$$

Here, mode amplitudes and phases are interpolated over r, the test particle's orbital radius. In order to recover the secular perturbation of P9 up to the specified order, one then has to average equation (A1) numerically over the test particle's orbital angle and a range of eccentricities, for any desired semi-major axis. In so doing, one first expresses harmonics in terms of orbital elements using

$$\begin{aligned} x = r\sin\theta\cos\phi &= r[\cos(\Omega - \varpi_{p9})\cos(\omega + f) \\ &\quad - \sin(\Omega - \varpi_{p9})\sin(\omega + f)\cos(i)], \end{aligned} \tag{A2}$$

$$\begin{aligned} y = r\sin\theta\sin\phi &= r\sin(\Omega - \varpi_{p9})\cos(\omega + f) \\ &\quad + \cos(\Omega - \varpi_{p9})\sin(\omega + f)\cos(i)], \end{aligned} \tag{A3}$$

$$z = r\cos\theta = r\sin(\omega + f)\sin(i). \tag{A4}$$

Then, one isolates functions of the true anomaly f, which are averaged numerically to yield

$$f_{l,m,n}(a,e) = \langle A_l^m(r)\cos(nf)\rangle, \tag{A5}$$

with $\langle\ \rangle$ standing for averaging over a test particle's orbit. Samples of the averaged functions $f_{l,m,n}(a,e)$ are shown in Fig. A1. We then transform from orbital elements to the vector notation using the

Downloaded from https://academic.oup.com/mnras/article/507/4/6078/6362616 by CNRS user on 20 April 2023

definition of the angular momentum and eccentricity vectors:

$$\boldsymbol{j} = \sqrt{1-e^2}\begin{pmatrix} \sin i \sin\Omega \\ -\sin i \cos\Omega \\ \cos i \end{pmatrix}, \tag{A6}$$

$$\boldsymbol{e} = e\begin{pmatrix} \cos\omega\cos\Omega - \sin\omega\cos i\sin\Omega \\ \cos\omega\sin\Omega + \sin\omega\cos i\cos\Omega \\ \sin\omega\sin i \end{pmatrix}. \tag{A7}$$

Using $\boldsymbol{e} = e\hat{u}$ and $\boldsymbol{j} = \sqrt{1-e^2}\hat{n}$, we can write the secular perturbation of P9 as

$$\begin{aligned}\bar{\Phi}_{\rm P9}(a,e) = {}& \Upsilon_0(a,e) + \Upsilon_1(a,e)e_u + \Upsilon_2(a,e)j_n^2 + \Upsilon_3(a,e)e_n^2 \\ & + \Upsilon_4(a,e)j_u^2 + \Upsilon_5(a,e)e_u^2 + \Upsilon_6(a,e)e_u j_n^2 \\ & + \Upsilon_7(a,e)e_n j_u j_n + \Upsilon_8(a,e)e_u e_n^2 + \Upsilon_9(a,e)e_u j_u^2 \\ & + \Upsilon_{10}(a,e)e_u^3,\end{aligned} \tag{A8}$$

with subscripts indicating the component of the particle's vectors along the basis vectors associated with the P9 plane, and with the functions $\Upsilon_i(a,e)$ given by

$$\begin{aligned}\Upsilon_0(a,e) = {}& -\frac{1}{\sqrt{4\pi}}f_{0,0,0} + \frac{1}{2}\sqrt{\frac{5}{16\pi}}[f_{2,0,0} - 3f_{2,0,2}] \\ & + \frac{1}{2}\sqrt{\frac{15}{32\pi}}\Big[f_{2,2,0} - 3f_{2,2,2}\Big], \\ \Upsilon_1(a,e) = {}& \frac{1}{e}\Bigg[\sqrt{\frac{3}{8\pi}}f_{1,1,1} + \frac{1}{4}\sqrt{\frac{21}{64\pi}}\Big[-f_{3,1,1} + 5f_{3,1,3}\Big] \\ & + \frac{3}{4}\sqrt{\frac{35}{64\pi}}\Big[f_{3,3,1} - 5f_{3,3,3}\Big]\Bigg], \\ \Upsilon_2(a,e) = {}& \frac{1}{1-e^2}\left[\frac{3}{2}\sqrt{\frac{5}{16\pi}}\Big[-f_{2,0,0} + f_{2,0,2}\Big]\right] + \frac{1}{2}\Upsilon_4(a,e), \\ \Upsilon_3(a,e) = {}& \frac{1}{e^2}\left[3\sqrt{\frac{5}{16\pi}}f_{2,0,2}\right] + \frac{1}{2}\Upsilon_5(a,e), \\ \Upsilon_4(a,e) = {}& \frac{1}{1-e^2}\left[\sqrt{\frac{15}{32\pi}}\Big[-f_{2,2,0} + 2f_{2,2,2}\Big]\right], \\ \Upsilon_5(a,e) = {}& \frac{1}{e^2}\left[2\sqrt{\frac{15}{32\pi}}f_{2,2,2}\right]\Bigg], \\ \Upsilon_6(a,e) = {}& \frac{1}{e(1-e^2)}\left[\frac{5}{4}\sqrt{\frac{21}{64\pi}}\Big[f_{3,1,1} - f_{3,1,3}\Big]\right] + \frac{1}{4}\Upsilon_9(a,e), \\ \Upsilon_7(a,e) = {}& 2\Upsilon_6(a,e), \\ \Upsilon_8(a,e) = {}& \frac{1}{e^3}\left[-5\sqrt{\frac{21}{64\pi}}f_{3,1,3} + 3\sqrt{\frac{35}{64\pi}}f_{3,3,3}\right], \\ \Upsilon_9(a,e) = {}& \frac{1}{e(1-e^2)}\left[3\sqrt{\frac{35}{64\pi}}\Big[-f_{3,3,1} + f_{3,3,3}\Big]\right], \\ \Upsilon_{10}(a,e) = {}& \frac{1}{e^3}\left[4\sqrt{\frac{35}{64\pi}}f_{3,3,3}\right]\Bigg].\end{aligned} \tag{A9}$$

A1 Equations of motion

Using equation (10), we derive the equations of motion for a test particle under the effect of the inner quadrupolar forcing from the giant planets and the outer forcing of the eccentric ring of P9, where the latter is driven by equation (A8). Taking the basis vectors of P9's orbit $\{\hat{u}_o, \hat{v}_o, \hat{n}_o\}$ as the reference triad, we have

$$\begin{aligned}L\frac{{\rm d}\boldsymbol{j}}{{\rm d}t} = {}& +\Gamma\frac{\boldsymbol{j}\cdot\hat{n}_{\rm p}}{\left(1-e^2\right)^{5/2}}(\boldsymbol{j}\times\hat{n}_{\rm p}) \\ & - \Big[2\Upsilon_2 j_n + 2\Upsilon_6 j_n e_u + \Upsilon_7 e_n j_u\Big](\boldsymbol{j}\times\hat{n}_{\rm o}) \\ & - \Big[\Upsilon_7 e_n j_n + 2\Upsilon_4 j_u + 2\Upsilon_9 e_u j_u\Big](\boldsymbol{j}\times\hat{u}_{\rm o}) \\ & - \Big[2\Upsilon_3 e_n + 2\Upsilon_8 e_u e_n + \Upsilon_7 j_u j_n\Big](\boldsymbol{e}\times\hat{n}_{\rm o}) \\ & - \Big[\Upsilon_1 + \Upsilon_6 j_n^2 + \Upsilon_8 e_n^2 + 2\Upsilon_5 e_u \\ & + \Upsilon_9 j_u^2 + 3\Upsilon_{10}e_u^2\Big](\boldsymbol{e}\times\hat{u}_{\rm o}),\end{aligned} \tag{A10}$$

$$\begin{aligned}L\frac{{\rm d}\boldsymbol{e}}{{\rm d}t} = {}& +\Gamma\frac{\boldsymbol{j}\cdot\hat{n}_{\rm p}}{\left(1-e^2\right)^{5/2}}(\boldsymbol{e}\times\hat{n}_{\rm p}) - \frac{\Gamma}{2}\frac{1-e^2-5(\boldsymbol{j}\cdot\hat{n}_{\rm p})^2}{(1-e^2)^{7/2}}(\boldsymbol{j}\times\boldsymbol{e}) \\ & - \Big[2\Upsilon_2 j_n + 2\Upsilon_6 j_n e_u + \Upsilon_7 e_n j_u\Big](\boldsymbol{e}\times\hat{n}_{\rm o}) \\ & - \Big[\Upsilon_7 e_n j_n + 2\Upsilon_4 j_u + 2\Upsilon_9 e_u j_u\Big](\boldsymbol{e}\times\hat{u}_{\rm o}) \\ & - \Big[2\Upsilon_3 e_n + 2\Upsilon_8 e_u e_n + \Upsilon_7 j_u j_n\Big](\boldsymbol{j}\times\hat{n}_{\rm o}) \\ & - \Big[\Upsilon_1 + \Upsilon_6 j_n^2 + \Upsilon_8 e_n^2 \\ & + 2\Upsilon_5 e_u + \Upsilon_9 j_u^2 + 3\Upsilon_{10}e_u^2\Big](\boldsymbol{j}\times\hat{u}_{\rm o}) \\ & - \Big[D_0 + D_1 e_u + D_2 j_n^2 + D_3 e_n^2 + D_4 j_u^2 + D_5 e_u^2 + D_6 e_u j_n^2 \\ & + D_7 e_n j_u j_n + D_8 e_u e_n^2 + D_9 e_u j_u^2 + D_{10}e_u^3\Big](\boldsymbol{j}\times\boldsymbol{e}),\end{aligned} \tag{A11}$$

where we have dropped the explicit dependence of Υ_i on a and e, and we have used $L = \sqrt{G{\rm M}_\odot a}$,

$$D_i(a,e) \equiv \frac{1}{e}\frac{{\rm d}\Upsilon_i(a,e)}{{\rm d}e}, \tag{A12}$$

and

$$\Gamma = \frac{3}{4}\frac{G{\rm M}_\odot}{a}\sum_{i=1}^{i=4}\frac{m_i a_i^2}{{\rm M}_\odot a^2}, \tag{A13}$$

with the sum taken over the four gaseous giants.

When considering coplanar dynamics, the Lenz vector equation reduces to

$$\begin{aligned}L\frac{{\rm d}\boldsymbol{e}}{{\rm d}t} = {}& \Bigg[\Gamma\frac{e}{\left(1-e^2\right)^2} \mp \Upsilon_1 l_{\rm p} + 2\Upsilon_2 e l_{\rm p} - 2\Upsilon_5 e l_{\rm p} \pm \Upsilon_6\left(3e^2-1\right)l_{\rm p} \\ & \mp 3\Upsilon_{10}e^2 l_{\rm p} - D_0 e l_{\rm p} \mp D_1 e^2 l_{\rm p} - D_2 e l_{\rm p}^3 - D_5 e^3 l_{\rm p} \\ & \mp D_6 e^2 l_{\rm p}^3 \mp D_{10}e^4 l_{\rm p}\Bigg]\hat{v}_{\rm o},\end{aligned} \tag{A14}$$

where $l_{\rm p} = |\boldsymbol{j}| = \sqrt{1-e^2}$ and upper/lower signs refer to apsidally aligned/anti-aligned configurations.

Downloaded from https://academic.oup.com/mnras/article/507/4/6078/6362616 by CNRS user on 20 April 2023

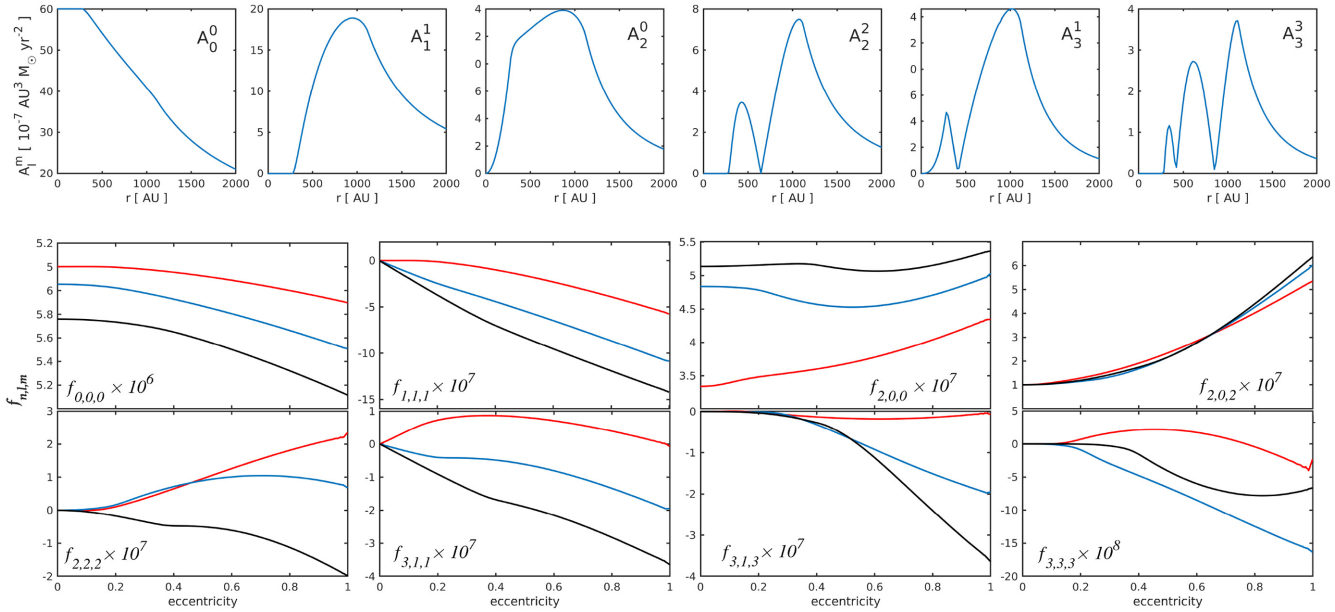

Figure A1. Orbit averaged harmonics and the potential of the P9 ring. Top row: Absolute values of the modes $A_l^m(r)$ used in the expansion of equation (A1). The modes decrease in amplitude as their harmonic degree increases, from the mostly dominant A_0^0 mode associated with the axisymmetric contribution, to higher harmonics corresponding to spatial asymmetries. Bottom rows: A sample of the numerically averaged functions $f_{l,m,n}(a, e) = \langle A_l^m(r)\cos(nf)\rangle$ used in the averaged potential in equation (A8). Each function is plotted for three values of the semi-major axis, namely: $a = 250$ au (red), 350 au (blue), 450 au (black). A color version of this figure is available in the online journal.

This paper has been typeset from a TEX/LATEX file prepared by the author.

Downloaded from https://academic.oup.com/mnras/article/507/4/6078/6362616 by CNRS user on 20 April 2023